nature biomedical engineering

Article

https://doi.org/10.1038/s41551-025-01439-z

Integration of chemical and physical inputs for monitoring metabolites and cardiac signals in diabetes

Received: 19 April 2024

Accepted: 22 May 2025

Published online: 2 July 2025

Check for updates

An-Yi Chang[1,2], Muyang Lin[1,2], Lu Yin[1,2], Maria Reynoso[1,2], Shichao Ding[1], Ruixiao Liu[1], Yuma Dugas[1], Ana Casanova[1], Geonho Park[1], Zhengxing Li[1], Hao Luan[1], Nelly Askarinam[1], Fangyu Zhang[1], Sheng Xu[1] ✉ & Joseph Wang[1] ✉

The development of closed-loop systems towards effective management of diabetes requires the inclusion of additional chemical and physical inputs that affect disease pathophysiology and reflect cardiovascular risks in patients. Comprehensive glycaemic control information should account for more than a single glucose signal. Here, we describe a hybrid flexible wristband sensing platform that integrates a microneedle array for multiplexed biomarker sensing and an ultrasonic array for blood pressure, arterial stiffness and heart-rate monitoring. The integrated system provides a continuous evaluation of the metabolic and cardiovascular status towards improving glycaemic control and alerting patients to cardiovascular risks. The multimodal platform offers continuous glucose, lactate and alcohol monitoring, along with simultaneous ultrasonic measurements of blood pressure, arterial stiffness and heart rate, to support understanding of the interplay between interstitial fluid biomarkers and physiological parameters during common activities. By expanding the continuous monitoring of patients with diabetes to additional biomarkers and key cardiac signals, our integrated multiplexed chemical–physical health-monitoring platform holds promise for addressing the limitations of existing single-modality glucose-monitoring systems towards enhanced management of diabetes and related cardiovascular risks.

Diabetes is a chronic disease characterized by elevated blood glucose levels that affects numerous people and leads to major complications[1,2]. Over the past two decades, continuous glucose-monitoring (CGM) systems have become the standard of care in managing diabetes[3–5]. Existing CGM systems rely on a needle-based subcutaneous enzymatic electrochemical biosensor that closely tracks the dynamics of glucose concentrations in the interstitial fluid (ISF)[5]. Such systems have evolved rapidly over the past two decades, showing impressive technological advances and capabilities towards optimal therapeutic interventions and improved glycaemic control[5]. Yet, all current commercial CGM systems are limited to the measurement of a single parameter (blood glucose concentration). Considering the complexity of diabetes, CGM platforms fall short of capturing the full spectrum of diverse symptoms experienced by people with diabetes and do not permit adequate response to glycaemic variability due to an unanticipated event, such as stress, meals or physical activity. Multiple studies have revealed the

[1]Aiiso Yufeng Li Family Department of Chemical and Nano Engineering, University of California San Diego, La Jolla, CA, USA. [2]These authors contributed equally: An-Yi Chang, Muyang Lin, Lu Yin, Maria Reynoso. ✉e-mail: shengxu@ucsd.edu; josephwang@ucsd.edu

benefit of monitoring additional biomarkers and physical inputs such as blood pressure (BP) and heart rate (HR) that affect insulin sensitivity for mimicking the physiological function of a healthy pancreas towards improving glycaemic control and understanding patient health[6–9]. Diabetes has also long been known to be associated with high risks of cardiovascular and kidney diseases[10,11]. The reduction of cardiac and nephropathy risks represents an important part of evaluating people with type 1 diabetes (T1D). Effective management of diabetes should thus include continuous monitoring of clinically relevant biomarkers in addition to blood glucose, and of multiple cardiovascular vital signals to understand the pathophysiology of diabetes and patient health with a view to reducing T1D-related complications and guiding personalized interventions.

Microneedle-based electrochemical sensors have been developed to enable continuous health monitoring at the molecular level using multiple chemical markers[12,13]. By continuously accessing the dermal ISF, the composition of which is very close to blood gold standard, minimally invasive sensing devices allow the real-time collection of important diagnostic information[14]. Microneedle arrays of multiple individually addressable sensing electrodes, functionalized with different receptors, can capture important dynamic chemical data through the simultaneous detection of many ISF biomarkers[14]. Although offering rich chemical information, such microneedle sensor arrays lack important information about key physical parameters relevant to the wearer's health and well-being. Critical real-time insights about dynamic changes in the wearer's cardiovascular status remain unchecked.

Multimodal wearable sensor systems, simultaneously monitoring multiple physical parameters and biochemical markers, have been introduced recently to address the limitations of current single-modality wearable chemical or physical sensors[15–18]. However, these multimodal wearable systems have focused solely on sweat-sensing epidermal patches. For example, earlier reports on integrated wearable hybrid sensing platforms have focused on the coupling of HR or BP sensors with single biomarker sweat sensors[15,16]. Sweat chemical sensors integrated with physical sensors that record skin temperature and galvanic skin response have been developed recently to monitor stress levels[18]. The scope and power of multimodal sensing platforms can be greatly enhanced by accessing the rich diagnostic biochemical information offered by the ISF, through simultaneous dynamic recording of multiple ISF biomarkers and with key cardiac physiological signals.

Here, we describe an integrated biomarkers-linked ultrasound electronic (BLUE) wristband platform, fusing the rich multiplexed chemical sensing capability of microneedle sensor arrays with critical physical sensors—namely, BP, electrocardiogram (ECG), HR and arterial stiffness—into a single flexible platform (Fig. 1a). The present BLUE platform addresses current technological gaps by combining multiplexed chemical sensing (including highly reliable continuous ISF glucose monitoring) with real-time detection of key physiological signals using a soft ultrasonic sensor array on a single soft wristband. The BLUE platform can thus track dynamic changes in metabolic and physical signals relevant to glucose metabolism and complications of diabetes, capturing the effects of transient stimulations, and uncovering correlations between daily activities and physio-metabolic responses. This chemical–physical combination enhances health monitoring and establishes the system as a versatile platform technology, offering a holistic view of the wearer's health. Here, we emphasize the importance of arterial stiffness, a key indicator of vascular health, measured via an ultrasound sensor—an innovation not previously explored in wearable sensors for diabetes.

The integrated BLUE platform has been carefully engineered to ensure reliable signal acquisition, eliminate crosstalk among its different sensing modalities and avoid signal drift under mechanical deformations. The microneedle array was designed to allow convenient replacement, so that the wear period could be tailored to minimize allergic reactions and risk of infection. The ability of the wristband system to measure multiple ISF chemical markers and physiological signals simultaneously and continuously was evaluated on multiple healthy participants and people with prediabetes during diverse daily activities, including food and drink intake and vigorous exercise. The presented hybrid system thus addresses the limitations of existing single-modality CGM devices and presents a unique opportunity for expanding the continuous monitoring of people with diabetes for additional biomarkers and key cardiac signals (BP, HR and arterial stiffness) associated with diabetes and related cardiovascular risks. This multimodal approach not only offers a more comprehensive assessment of people with diabetes, but also lays the foundation for integrating on a single device the monitoring of key vital signs along with the biosensing of multiple ISF biomarkers. This ability to generate rich multisource chemical–physical data is particularly attractive for optimal personalized inulin dosing in a closed-loop diabetes system.

Results

Design of the microneedle and ultrasound sensor modules

Rational selection of specific sensing modules depends on the target user group and corresponding diagnostic requirements. Figure 1b(i) illustrates penetration of the microneedle from the epidermis to the dermis, using a microneedle length of 800 µm, which ensures the biomarker-rich dermis layer is reached. The ultrasound sensor's transducer measured the pulse–echo simultaneously from the blood vessel (Fig. 1b(ii)). Placing the flexible microneedles and ultrasound sensors on a flexible polyethylene terephthalate substrate provides the necessary close skin contact and comfort, without displacing or losing skin contact during diverse daily activities, including vigorous exercise. Additional experiments were performed to demonstrate the robust contact between the skin and wristband during physical activity (Supplementary Fig. 1 and Supplementary Videos 1–3). The data illustrate the mechanical integrity of the wristband under different bending angles during common outdoor activities, such as doing push-ups, playing basketball and jumping rope.

Figure 1c shows a healthy participant wearing the multimodal BLUE platform. There are two ECG electrode pads. The pad on the inside of the wristband is connected to the wearing hand, while the pad on the outside is touched using a finger from the non-wearing hand to measure the potential difference across the heart (Fig. 1c(i)). The multiplexed microneedle sensor array is worn tightly over the wrist to ensure facile and reliable skin penetration. Figure 1c(ii) is an inverted view of the band, showing the microneedles with a flexible three-dimensional (3D)-printed adaptor and holder. Ultrasound sensors are located on the top of the wrist pulses to measure the pulse–echo. An array of 10 ultrasound sensors (3 × 1 cm in area) were designed to address issues of dislocation and signal loss (Fig. 1c(iii) and Supplementary Videos 4 and 5). The individual sensor modalities were fabricated on a polyethylene terephthalate substrate and are spatially separated from each other on the same wristband (Fig. 1c(iv)), to prevent sensor crosstalk.

A smart device displays the continuous response of the individual sensors, with simultaneous recording of BP, ECG, HR and three biomarkers (glucose, alcohol and lactate) to provide insights into the influence of daily activities on metabolic and physiological processes (Fig. 1d(i)). By capturing and processing large amounts of personal data, the smart device is able to provide a personal digital health status summary. We can also use machine learning prediction algorithms to alert for potential abnormalities. The performance of the multimodal wristband was first demonstrated for continuous real-time glucose monitoring using biocompatible SU-8-based microneedle biosensors over a period of 70 min and was compared with parallel testing using a blood glucose meter (BGM) and CGM at 10- and 5-min intervals, respectively. The corresponding BP and HR signals were collected simultaneously (Fig. 1d(ii)) using the

https://doi.org/10.1038/s41551-025-01439-z

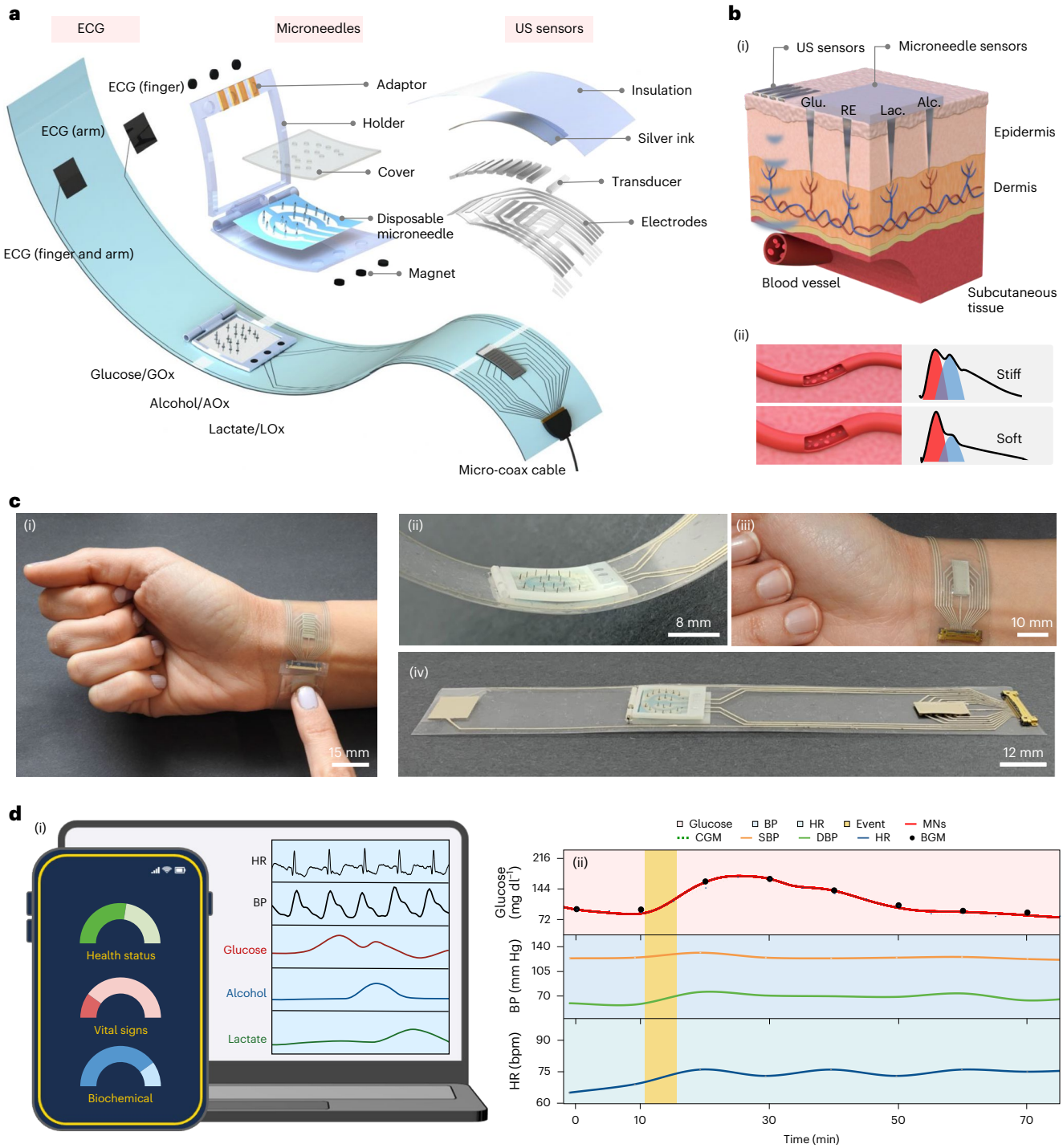

Fig. 1 | Overview of the multimodal BLUE platform for simultaneously tracking chemical biomarkers and physical signals. a, The hybrid monitoring system integrates a multiplexed microneedle array that simultaneously measures multiple ISF chemical markers (glucose (Glu.), alcohol (Alc.) and lactate (Lac.)) via the corresponding oxidase-based recognition reactions and amperometric signal transduction. The embedded sensors for physiological signals include ultrasound BP transducers and customized silver ink printed biopotential electrodes (ECG). BP during movements was measured via 10 ultrasound sensors with an area of 3 × 1 cm. Headings indicate the corresponding regions of the wristband, including the ECG, microneedles (MN) and ultrasonic sensors. **b**, (i) Cross-section of the skin with the microneedle array and ultrasound (US) sensor array. The microneedles penetrate from the stratum corneum of the epidermis to the dermis for ISF biosensing, providing continuous current signals related to concentrations of blood glucose, alcohol and lactate. BP, HR and arterial stiffness can be decoded from the change in vessel diameter. (ii) Changes in vessel diameter with different morphology showing stiff (upper) and soft (lower) arteries. **c**, Multimodal monitoring system on a participant's wrist (ECG) (i), an individual inverted microneedle sensor array (ii) and ultrasound BP transducers (iii) along with the entire wristband (iv). **d**, (i) A laptop displays parallel signal recording of the ultrasound sensors for BP and the microneedles of three biomarker readings (glucose, alcohol and lactate). The device processes the multisource data, displays and summarizes digital health status using key parameters, and alerts for potential abnormalities. Values of the data points for each sensor are recorded in real time. (ii) Comparison of real-time microneedle glucose monitoring (data points per s; in red) with the response of the glucose blood meter (data points per 10 min; black) and CGM (data points per 1 min; dotted line), over an 80 min period, along with simultaneous recording of HR and BP, which include diastolic blood pressure (DBP) and systolic blood pressure (SBP). A soft drink was taken after the first 10 min (yellow box). AOx, alcohol oxidase; GOx, glucose oxidase; LOx, lactate oxidase; RE, reference electrode.

https://doi.org/10.1038/s41551-025-01439-z

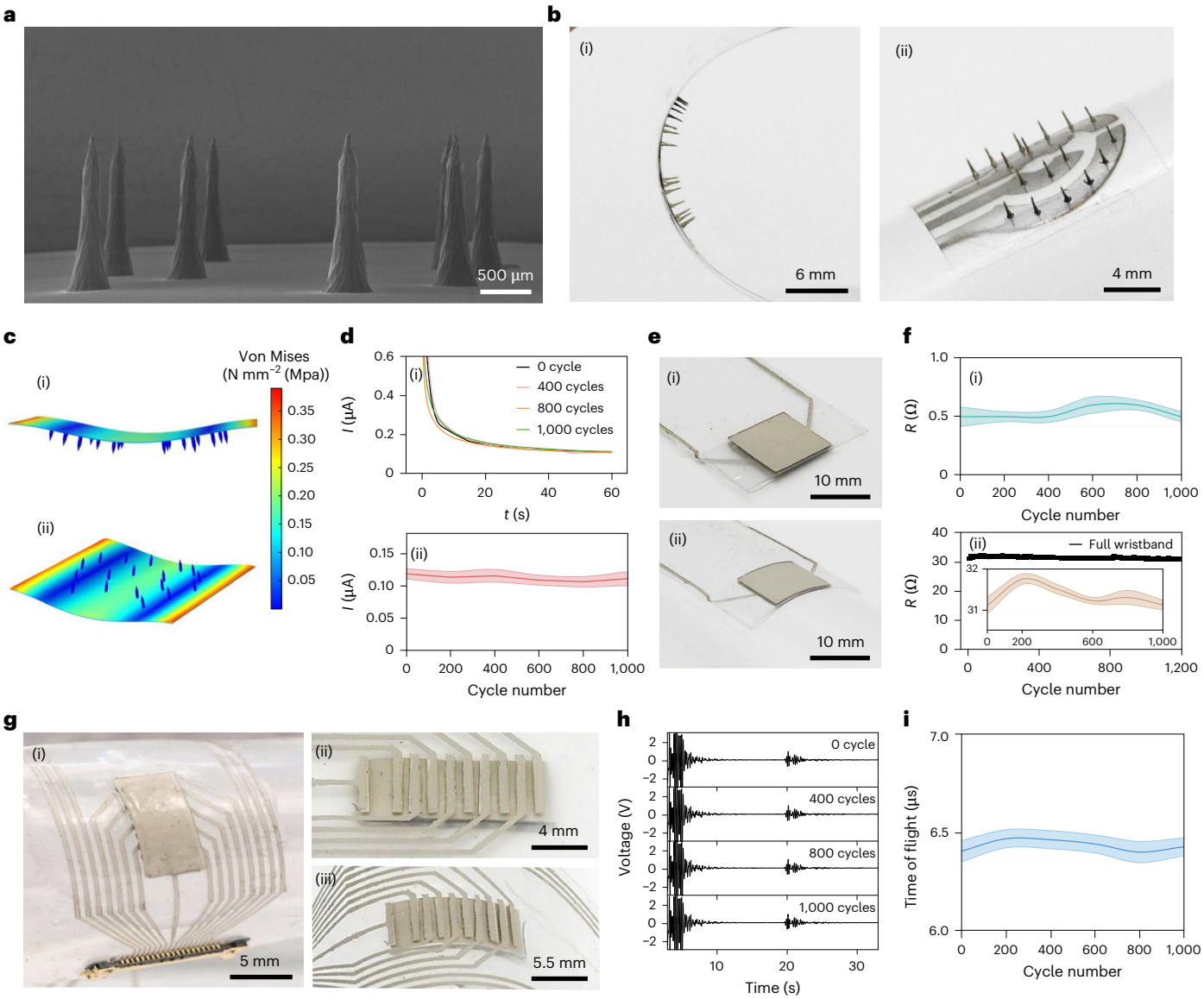

Fig. 2 | Mechanical properties of the sensing platforms. a, Scanning electron microscopy image of the bare microneedles after 60 min of dry etching. The microneedles were independently fabricated three times on glass slides. **b**, Microneedle bending after sputtering of Cr (200 nm) and Pt (300 nm) layers: (i) inward 0.35 rad bending and (ii) outward 0.35 rad bending. **c**, Simulation of the microneedle flexural strength using a force of 20 N m^{-2} on the back (i) and top (ii) of the microneedles. **d**, Electrochemical performance upon bending 1,000 times. (i) Chronoamperometry signals measured at 0, 400, 800 and 1,000 cycles. (ii) Currents measured every 200 cycle counts with 0.3 V for 60 s. Error is indicated by shading around the curve. For error bars $n = 5$. Data are presented as mean ± s.d. **e**, ECG before (i) and after (ii) bending by 0.35 rad. **f**, (i) Biopotential electrode resistance measured on the two edges every 200 cycles during 1,000 bending cycles. For error bars, $n = 5$. (ii) Full wristband resistance (silver ink printed connection wires) measured during 1,000 cycles at resistance points of each 200 cycles. For error bars $n = 5$ and data are presented as mean ± s.d. **g**, Photographs of (i) the ultrasound sensors before (ii) and after (iii) 20° bending. **h**, Pulse–echo measured at 0, 400, 800 and 1,000 cycles. **i**, Bending of the ultrasound sensors at 0.35 rad up to 1,000 times, with pulse–echo measurements every 200 cycles. For error bars $n = 5$ and data are presented as mean ± s.d.

integrated ultrasound and ECG sensors, respectively. A glucose-rich soft drink was taken after the initial 10 min. Note that the microneedle sensor and CGM responded identically to intake of the drink, with their response increasing with glucose level for 20 min and returning to baseline for a total of 50 min. The excellent agreement between the ISF-based microneedle glucose sensor and the BGM is reflected by a mean absolute relative difference (MARD) value of 4.68%. The CGM also shows good agreement with the BGM measurements, with a MARD of 5.40%. The highly accurate CGM capability of the microneedle sensing system is coupled with simultaneous recording of the changes in BP and HR (Fig. 1d(ii)). The integrated physical sensors show that both BP and HR increased with the change in blood glucose, suggesting dynamic responses to diverse daily activities. In addition, arterial stiffness, a critical parameter in the evaluation of vascular health, is also responsive to daily activities.

With the rich metabolic ISF profile captured by the multiplexed microneedle array and simultaneous ultrasound recording of BP and HR, the BLUE system offers wearers continuous real-time insights into the dynamics of their physiology, for personalized health, wellness and nutrition. The wristband platform has distinct advantages for continuous monitoring of different age groups, ranging from neonates (type 1) to older adults (types 1, 2 or both), including people with underlying health conditions or at-risk populations, such as people with cardiac disease, sepsis or diabetes (Supplementary Fig. 2). For example, simultaneous BP and lactate measurements are important predictors of a range of life-threatening complications from septic

shock to open-heart surgery[19,20]. The hybrid BLUE platform can be tailored to meet the demands of wearers from diverse populations. By combining abundant metabolic ISF biochemical signals (from the multiplexed microneedle array) with ultrasound-based cardiovascular signals, the wristband platform offers rich dynamic insights into the health and physiological status of individuals with a view to maintaining their health and managing chronic diseases. Future incorporation of advanced data-processing clustering and classification techniques would offer timely alerts for abnormalities and predict disease onset.

Microneedle fabrication

The flexible microneedle array was fabricated using a combination of 3D printing[21], dry etching[22] and soft lithography[23] (Supplementary Fig. 3). We addressed the challenge of fabricating flexible SU-8 microneedles with a tip diameter <10 µm and length >800 µm, as needed to penetrate the skin and reach the biomarker-rich dermis. A 3D printer was used to fabricate the first microneedle mould to address the length challenge and SU-8-coating thickness limitations of photolithography (Supplementary Fig. 3). Polydimethylsiloxane (PDMS) was applied to the 3D-printed microneedles and cured for 1 h at 60 °C. The limited resolution of the 3D-printed microneedles resulted in a tip diameter of 215.80 ± 29.21 µm. A dry-etching process was introduced to improve the tip diameter. By increasing the etching time from 30 min to 45 and 60 min (Supplementary Table 1), we obtained the desired microneedles (Supplementary Fig. 4 and Supplementary Discussion 1). In particular, 60 min of etching resulted in a tip diameter of around 5–10 µm and a needle length of >1 mm (Fig. 2a)[24], which offers smooth skin penetration without breaking the microneedle, via a biocompatible material (Supplementary Fig. 5 and Supplementary Discussion 2). The second PDMS mould was cast using etched microneedles for subsequent fabrication of SU-8 microneedles via a soft lithography technique[21] (Supplementary Fig. 3). The flexibility of the microneedle with a tape substrate was demonstrated by an inward bend of 0.35 rad (Fig. 2b(i)) and outward bend of 0.35 rad (Fig. 2b(ii)), along with 0.79 rad of outward and inward bending (Supplementary Fig. 6a) for the assembly cover with the microneedles (Supplementary Fig. 6b). The flexibility of the cover, holder and adaptor were also demonstrated in a bending test (Supplementary Fig. 7), together with a side-by-side comparison of the size of the microneedle and full wristband using a penny coin for reference (Supplementary Fig. 6c,d). After sputtering of Cr (188.40 ± 26.87 µm) and Pt (337.76 ± 44.08 µm) layers, the microneedles maintained their flexibility with 0.35 rad bending (Supplementary Fig. 8). On being fully bent around participants' wrists, we found an average bending angle of 0.31 rad, with a minimum of 0.26 rad and a maximum of 0.35 rad across 20 participants. The adjustable mechanical properties enhanced the sensing signals, while ensuring comfort without the sensation of wearing a rigid foreign object (Supplementary Fig. 9). To evaluate further the effects of bending, we included a new experimental set-up demonstrating that signal acquisition across all sensing modalities remains reliable despite bending and the motion of the wrist (Supplementary Fig. 10).

Mechanical performance of the sensing platforms

The mechanical properties of flexural strength were simulated by applying a pressure of 1,000 N m^{-2} in the outward and inward directions, along with surface forces distribution during microneedle skin penetration (Fig. 2c(i,ii), Supplementary Figs. 11–14, Supplementary Discussion 3 and Supplementary Video 6). This revealed the surface stress maps, with the highest stress on the edge and in the centre of the microneedle. The microneedle design therefore avoided damage by preventing direct pressure on the high-pressure area. The required microneedle penetration pressure is around 0.1–3 N. The tip integrity of the microneedle was maintained after skin penetration (Supplementary Fig. 5); the SU-8 tensile strength is 60 M N m^{-2} on the SU-8 2000 series[25]. The robust performance of the microneedles, biopotential electrodes, full wristband and ultrasonic array under deformation were validated using 1,000 repeated 0.35-rad bends, indicating that the Pt-coated microneedles could maintain reliable performance on a flexible substrate (Fig. 2d(i,ii)). Figure 2e(i.ii) illustrates the flexibility of the biopotential ECG electrodes, which maintain valid readings with few resistance fluctuations of 0.5 Ω (Fig. 2f(i)). The full wristband maintains a resistance of 31 Ω (Fig. 2f(ii)). Scanning electron microscopy images indicate no notable surface damage (Supplementary Fig. 15). The ultrasonic array was fabricated using transfer printing methods[26], and this flexible structural design allows a bend of 0.35 rad, as shown in Fig. 2g(i–iii), along with sensor robustness, which was assessed under a bending test comprising 1,000 repetitive bends (Fig. 2h,i).

Crosstalk study

It is critical to avoid crosstalk effects between the different sensing modalities. To assess potential crosstalk, we evaluated first the influence of the physiological sensors on the performance of the electrochemical microneedle sensor array for the smallest size of wristband (125 mm). Wristbands were manufactured in three sizes: 125, 145 and 165 mm (Supplementary Fig. 16). Continuous microneedle current signals were recorded while switching the ECG and BP on and off repeatedly every 30 s (Fig. 3a,b). On separating the ECG, BP and microneedle modalities by 3 cm, the ECG and BP displayed minimal current peak noise. The crosstalk resiliency of the ECG measurements was investigated by switching the microneedles and BP on and off repeatedly every 3 s during the ECG measurements. The results indicate that the ECG readings are not affected by electrochemical and acoustic BP operations (Fig. 3c,d). Placing the ECG sensors 5 and 3 cm from the microneedle and BP sensors, respectively, eliminates such crosstalk. Similarly, the ultrasonic sensor is not affected by switching the microneedles and ECG sensors on and off repeatedly every 3 s during BP measurements (Fig. 3e,f). By spatially separating and isolating the individual sensor modalities, the integrated wristband system offers a stable multimodal wearable sensor performance, with no apparent crosstalk.

Arterial stiffness and compliance study

Arterial compliance can be extrapolated from the BP waveform by calculating the augmentation index (AIx). The BP waveform profile shows variations before and after exercise, reflecting changes in systemic vascular resistance throughout the whole arterial tree (Fig. 3g). AIx, defined as the difference between the systolic peak and the augmented peak ($P_1 - P_2$), normalized by the systolic peak (P_1), can act as a suitable metric to characterize arterial compliance (Fig. 3h). Average AIx increased from an initial value of 0.08 ± 0.04 before exercise to 0.25 ± 0.06 after exercise because of vasodilation, reflecting the effect of exercise on arterial stiffness.

Reliability and accuracy of biomarker sensing

Reliable, accurate, stable biomarker responses and biocompatibility (Supplementary Fig. 17) are essential to pave the way for on-body measurements, considering the potential complications of surface biofouling and enzyme stability during extended sensing operations. In addition, individual microneedle sensors—for glucose, alcohol and lactate—were characterized in vitro for their sensitivity, selectivity and stability in phosphate-buffered saline (PBS) (Supplementary Fig. 18) and artificial ISF (Supplementary Fig. 19s and Supplementary Discussion 4). The body normally maintains specific metabolite concentration ranges, such as 3.9–5.5 mmol l^{-1} glucose and 0.5–2.2 mmol l^{-1} lactate. Continuous individual measurements of glucose, alcohol and lactate were collected while the participant was drinking a soft drink, drinking wine and undertaking with vigorous-intensity exercise, respectively. Excellent agreement was observed between trends in the on-body wristband multiplexed microneedle data and the readings of commercial metabolite blood meters (Supplementary Fig. 20). The results suggest that the individual biomarker microneedle sensors offer highly accurate and reliable long-term monitoring.

https://doi.org/10.1038/s41551-025-01439-z

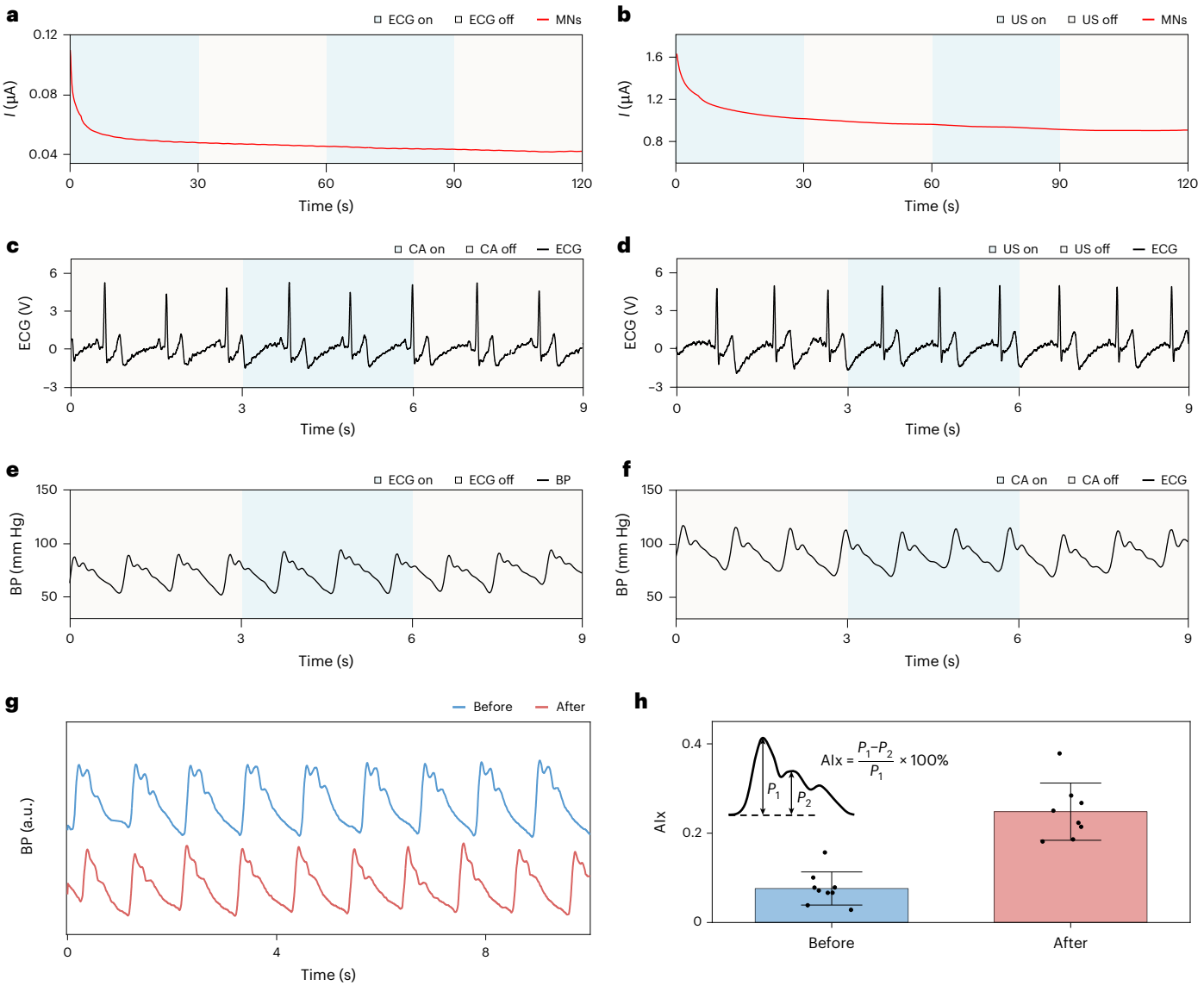

Fig. 3 | Monitoring and characterization of individual sensors. a,**b**, Crosstalk of the electrochemical signals of chronoamperometry (CA) to ECG (**a**) and ultrasound (US) (**b**). **c**,**d**, Crosstalk of ECG to the CA (**c**) and US (**d**). **e**,**f**, Crosstalk of ultrasound to ECG (**e**) and CA (**f**) signals. **g**, BP waveforms before and after exercise, which induced changes in the arterial compliance (the top and bottom pressure waveforms represent before and after exercise, respectively). **h**, AIx derived from the systolic peak (P_1) and augmented peak (P_2) values in the BP waveform ($n = 8$). Data are presented as mean ± s.d. Average AIx increased from 0.08 ± 0.04 before exercise to 0.25 ± 0.06 after exercise, suggesting decreased arterial stiffness.

On-body monitoring with a single daily activity stimulation

The hybrid BLUE platform was tested in multiple on-body trials in healthy participants who performed various daily activities. The wristband was used to acquire multiple chemical signals, including glucose, alcohol or lactate, and physiological signals, including BP, HR and arterial stiffness, to examine the complex response of participants to different stimulations; for example, eating food, drinking alcohol or taking exercise, and the skin recovery rate (Supplementary Figs. 21 and 22 and Supplementary Discussions 5–7).

Measurement of fasting and postprandial glucose levels is important for people with diabetes towards adjusting their medication, diet and lifestyle. Hypoglycaemia can often be associated with symptoms of hunger, dizziness, rising HR, confusion, diaphoresis and syncope, whereas the intake of sugar after fasting may induce postprandial hyperaemia that leads to an increase in arterial stiffness[27]. The ability of the BLUE platform to record a person's response to the same food intake was examined by monitoring the ISF glucose level along with physiological signals. Monitoring was undertaken in a healthy participant who consumed the same food in two separate on-body trials after fasting for >8 h overnight versus eating a meal within 4 h before the trial. Although preprandial glucose levels (87 and 86 mg dl^{-1}) were similar, glucose levels rose to 166 mg dl^{-1} with >8 h fasting and to 133 mg dl^{-1} without fasting, after eating the same food at a different meal frequency (Fig. 4a)[28]. Simultaneously, the preprandial BP level at fasting (107/59 mm Hg) was lower than that without fasting (113/62 mm Hg), while the artery was less stiff after fasting (AIx = 0.37 ± 0.04) than in the non-fasting group (AIx = 0.26 ± 0.06). Reduced arterial stiffness with fasting may be caused by dilation of the vascular system to accommodate blood volume depletion, reflecting that fasting benefits the elasticity of the vascular system, which can potentially mitigate or delay vascular ageing and reduce cardiovascular risks. After food intake, both trials showed an increase in BP, with the fasting group displaying a greater BP increase (132/80 mm Hg) than the non-fasting group (127/71 mm Hg). This investigation demonstrates the interplay of blood glucose, HR and BP under non-fasting and fasting conditions. In both trials, the MARD value of the microneedle glucose sensor versus BGM

was 2.16% (26 paired data points), reflecting the high accuracy of the microneedle sensing platform.

Ingestion of alcohol is associated with a decrease in BP because of its vasodilation effect. Yet, extended, excessive alcohol ingestion is shown to significantly increase BP and arterial stiffness[29]. Furthermore, alcohol ingestion often has a complex interplay with different diseases. The population with diabetes has a higher risk of hypertension, even from moderate ingestion of alcohol[30]. Alcohol tolerance also varies between individuals. For non-drinkers, alcohol consumption can cause more narrowing of the blood vessels, which leads to increased BP and HR[31]. The integrated wristband can be used to track an individual's alcohol intake along with the corresponding cardiovascular responses. Here, two on-body trials were conducted comparing the responses of a healthy habitual drinker and a non-drinker to an identical alcohol-ingestion stimulation. Figure 4b displays the ISF alcohol profiles for two participants over 2 h after drinking equal amounts of alcohol. The drinker and non-drinker demonstrated blood alcohol concentrations falling at 3.29 and 3.93 mmol h^{-1}, with highest blood alcohol levels of 0.043% and 0.053%, respectively. Such microneedle alcohol sensing leads to a MARD of 8.84% compared with a commercial breathalyser (26 paired data points). Note that in response to the alcohol, the non-drinker showed an increase in BP from 78 to 109 mm Hg, and in HR from 62 to 70 bpm, along with reduced AIx by vasoconstriction from 0.20 ± 0.02 at 0 min to 0.13 ± 0.04 at 30 min. By contrast, alcohol had a negligible effect on the BP, HR and arterial stiffness of the drinker. The non-drinker had a lower arterial stiffness than the drinker (AIx of 0.17 ± 0.02), consistent with the effect of alcohol consumption on increasing arterial stiffness[32]. Overall, in this trial, the wristband device provided real-time quantitative alcohol, BP, HR and arterial stiffness data for comprehensive assessment of the individual's response to alcohol consumption.

Vigorous-intensity daily exercise has benefits in reducing the onset of various cardiovascular diseases[33]. Exercise induces rapid metabolic and cardiac changes, with the responses highly dependent on an individual's fitness and activity levels[34]. In addition to HR and BP, lactate is one of the most commonly tracked indicators that reflects an individual's training intensity or related diseases of cardiogenic shock, liver failure and sepsis. High-intensity training improves athletic performance by increasing the indicators of lactate threshold, which relates to the lactate clean rate[35]. To demonstrate the ability to track individuals with different fitness levels, an athlete and a non-athlete conducted 20 min of intense exercise, while comparing their continuous microneedle lactate response with that of a commercial blood lactate monitor. The non-athlete participant exercised fewer than 3 days per week, for 30–60 min per day with a total of less than 6–12 h of exercise per month. By contrast, the athlete participant undertook 4 h of training per day, 20 h per week with a total of 80 h of exercise per month. The non-athlete had a greater increase in the lactate level from 1.78 to 8.67 mM after 10 min of exercise, and to 10.22 mM after 20 min of exercise (0.98 J s^{-1}) (Fig. 4c). In comparison, the lactate level for the athlete increased from 2.89 to 6.33 mM after 10 min of exercise and to 8.56 mM after 20 min of exercise (1.00 J s^{-1}). After stopping the exercise, the lactate level decreased for both participants, with that of the non-athlete dropping to 2 mM lactate within 10 min and to the rest baseline of 2.89 mM after 30 min rest. By contrast, the athlete displayed a faster lactate clearance rate, dropping to 4.89 mM within 10 min and to the rest baseline (2.78 mM) within 20 min. Along with these real-time lactate measurements, the BLUE platform offers convenient continuous monitoring of key physiological signals, giving simultaneous insights into the cardiac and metabolic effects of exercise. For example, after 20 min of exercise, the athlete demonstrated a higher BP of 179/96 mm Hg compared with the non-athlete (131/49 mm Hg), along with a lower HR of 115 bpm compared with that (128 bpm) of the non-athlete. The non-athlete displayed a reduced BP (102/62 mm Hg at 60 min to 98/47 mm Hg at 140 min) and arterial stiffness (AIx of 0.19 ± 0.04 to 0.32 ± 0.04) after 10 min of exercise. The wristband device can track BP dynamics during exercise (as high as 179/96 mm Hg for the athlete participant and post-exercise hypotension 131/49 mm Hg for the non-athlete), indicting its promise as an effective tool for alerting exercise-related hypertension[36] and post-exercise hypotension[37]. The lactate microneedle sensing provided a MARD value of 7.97% compared with the blood lactate meter (26 paired data points).

On-body monitoring with multiple daily activity stimulations

The BLUE system was tested on healthy participants performing diverse activities for 220 and 400 min to assess and understand the body's response during different daily stimulations. Full details of the experimental set-up are included in Supplementary Fig. 23. The performance and accuracy of the wristband microneedles for continuous glucose monitoring were compared with that of commercial CGM and BGM via two glucose-rich stimulations, along with simultaneous measurements of BP, HR and arterial stiffness (Fig. 5a(i–iii) and Supplementary Figs. 24–26). Following initial stabilization and 30 min of baseline recording, glucose levels started to increase with the food intake at 60 min, while the BP and HR increased from 110/62 mm Hg and 58 bpm (at 60 min) to 129/78 mm Hg and 71 bpm (at 70 min), respectively. The averaged AIx decreased from 0.211 ± 0.05 (at 60 min) to 0.175 ± 0.06 (at 70 min). The glucose level reached its highest value of 156 mg dl^{-1} (8.67 mM) at 100 min, along with BP and HR values of 113/59 mm Hg and 76 bpm. Subsequently, the glucose readings of the three systems decreased with time, reaching 106 mg dl^{-1} at 170 min, along with BP and HR readings of 116/64 mm Hg and 70 bpm, respectively, and an average AIx increase to 0.223 ± 0.03. Upon the intake of iced tea at 170 min, the glucose level started to increase again, while the BP and HR

Fig. 4 | In vivo monitoring of BP along with different biomarkers. a, (i) ISF glucose concentrations, BP and HR level for a non-fasting participant in response to eating a complete meal. (ii) Eight seconds of BP signals were recorded and (iii) mean AIx values were calculated at 0 and 30 min. For error bars, $n = 7$, and data are presented as mean ± s.d. (iv) ISF glucose concentrations, BP and HR level of an 8-h fasting participant in response to eating a complete meal. (v) Eight seconds of BP signals were recorded and (vi) mean AIx values were calculated at 0 and 30 min. For error bars, $n = 7$. The wristband results were compared with results using commercial BGM and BP monitors at 10 min. The BP waveform and AIx before and after the meal indicate elevated BP and arterial stiffness values. **b**, (i) ISF alcohol, BP and HR level of a non-drinker participant in response to a glass of wine (150 ml, 13.5% alcohol). (ii) Eight seconds of BP signals were recorded and (iii) corresponding mean AIx values were calculated at 0 and 30 min. For error bars, $n = 7$ and data are presented as mean ± s.d. (iv) ISF alcohol, BP and HR level of a drinker participant in response to a glass of wine (150 ml, 13.5% alcohol) over 140 min. (v) Eight seconds of BP signals were recorded and (vi) corresponding mean AIx values were calculated at 0 and 30 min. For error bars, $n = 7$. The wristband results were compared with results from a breathalyser and a commercial BP monitor at 10 min. The BP waveform before and after the alcohol intake indicates elevated BP levels in both participants, while the AIx indicates that the non-drinker has a significant increase in arterial stiffness compared with the drinker. **c**, (i) ISF lactate, BP and HR level of a non-athlete participant in response to vigorous-intensity exercise. (ii) Eight seconds BP signals were recorded before exercise (at 0 min) and 30 min after exercise and (iii) corresponding mean AIx values were calculated at 0 and 30 min. For error bars, $n = 7$, and data are presented as mean ± s.d. (iv) ISF lactate, BP and HR levels of an athlete participant in response to 20 min of vigorous-intensity exercise. (v) Eight seconds of BP signals were recorded before exercise (at 0 min) and 30 min after exercise and (vi) corresponding mean AIx values were calculated at 0 and 30 min. For error bars, $n = 7$. The wristband results were compared with results from a a blood lactate meter and an arm BP monitor every 10 min. The BP waveform, before and after the exercise, indicates elevated BP levels in both participants, while the AIx change indicates that the non-athlete has a greater decrease of arterial stiffness than the athlete. BLM, blood lactate meter.

https://doi.org/10.1038/s41551-025-01439-z

increased to 127/69 mm Hg and 71 bpm, and the average AIx decreased to 0.202 ± 0.04 (at 180 min). Overall, the microneedles displayed similar glucose trends compared with the corresponding blood glucose levels and CGM profiles, with good accuracy, as indicated by the Parkes error grid[38]. The first grid compares the microneedle glucose measurements with those of BGM, with all 158 points (100%) in zone A (Fig. 5a(iv)). The second grid compares the CGM measurements with the BGM readings, with all (100%) of the points in zones A + B (71 points), including 98.59% in zone A and 1.41% in zone B (Fig. 5a(v)). The MARD value of the microneedles glucose sensor compared to the CGM was 6.58%

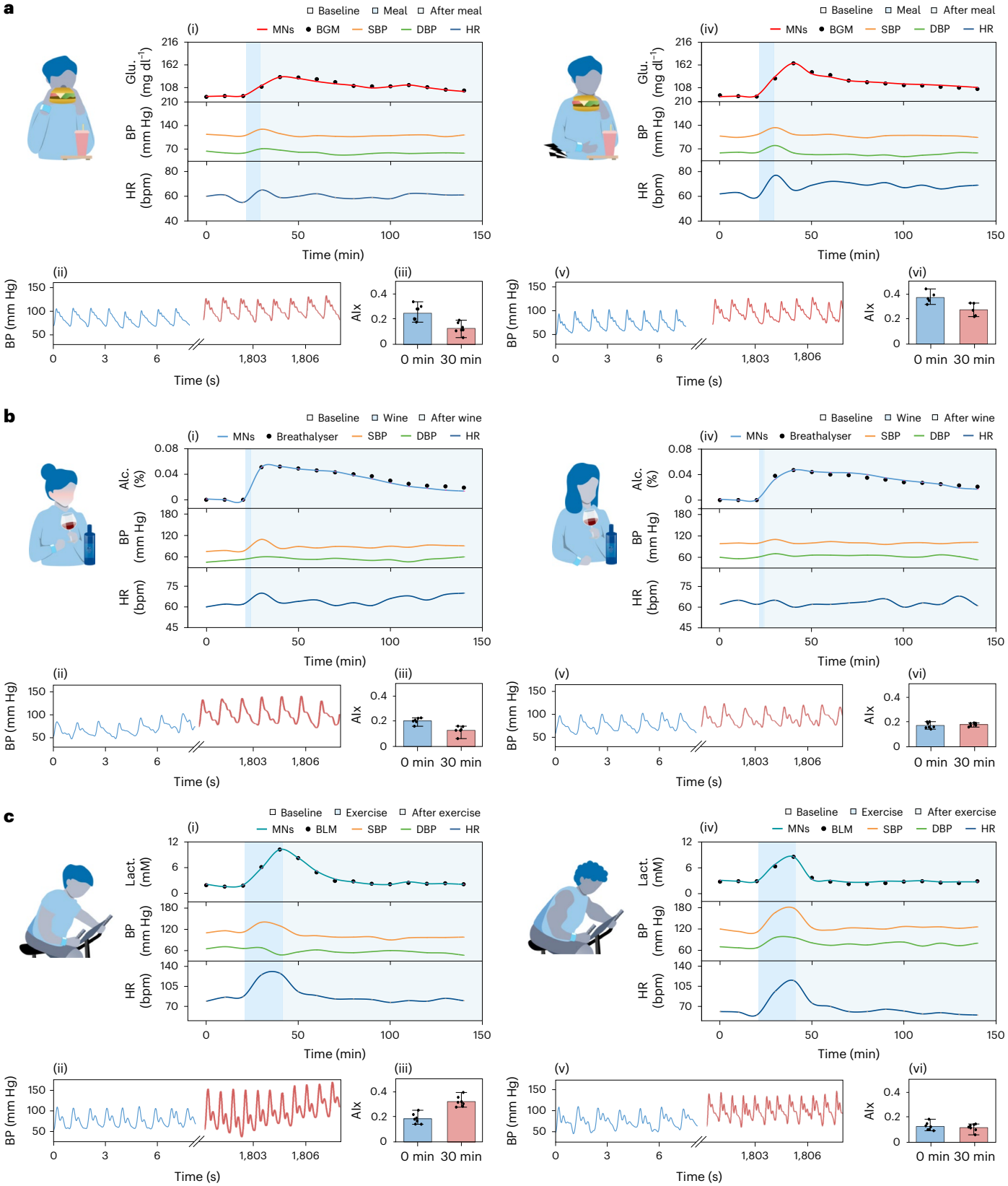

https://doi.org/10.1038/s41551-025-01439-z

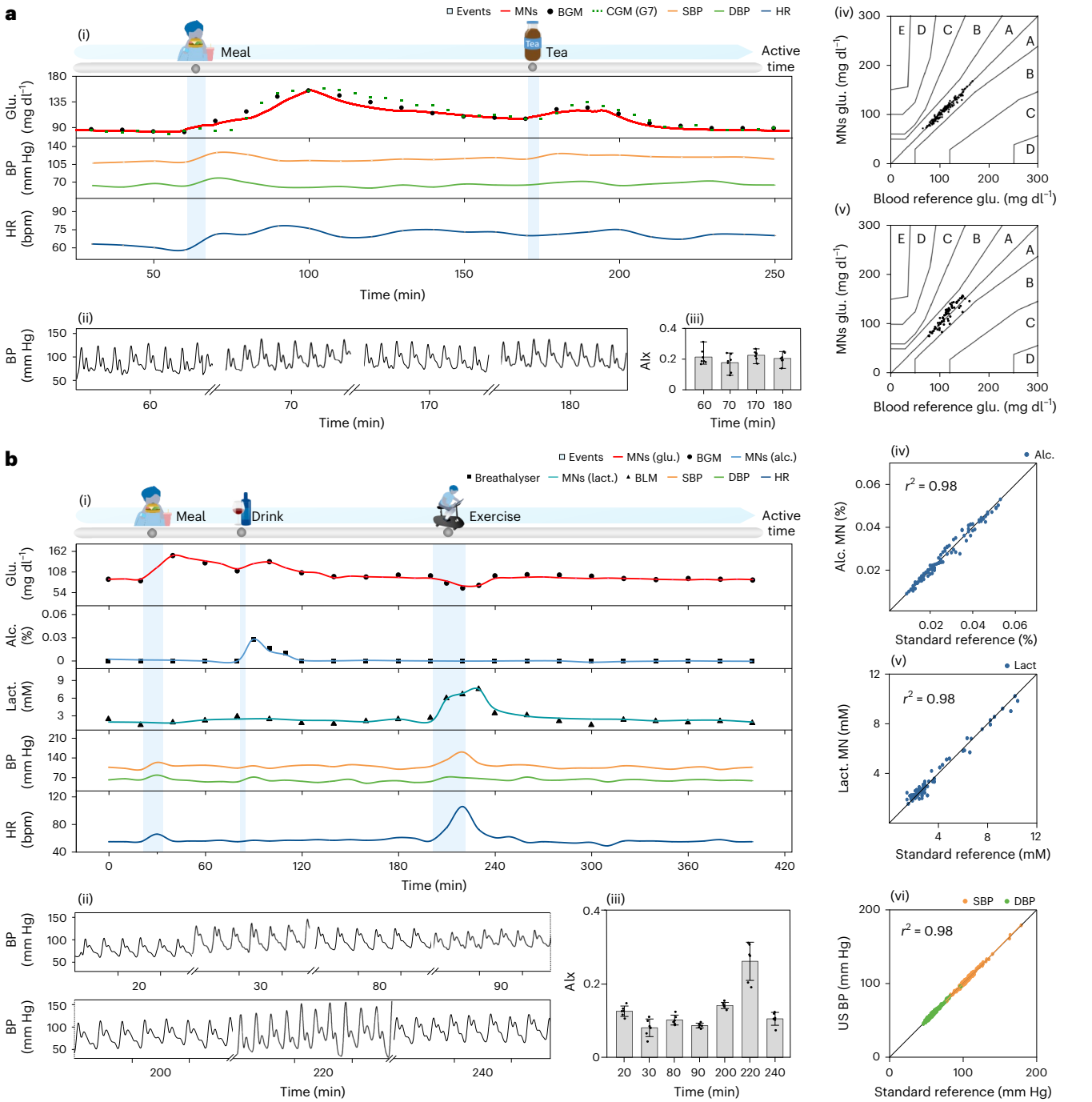

Fig. 5 | Extended simultaneous in vivo monitoring BP along with multiple biomarkers during different daily activities. a, Glucose monitoring before a meal for 30 min and after a meal for 3 h via two stimulations. First a meal was eaten at 60 min and second a cup of iced tea was drunk at 170 min. (i) Comparison of ISF microneedle glucose monitoring (every 1 s) against glucose measurements with CGM (every 5 min) and BGM (every 10 min), along with simultaneous monitoring of BP and HR. (ii) The participant's 8 s BP data recorded before a meal at 60 min, after a meal at 70 min, before a cup of tea at 170 min and after a cup of tea at 180 min. (iii) AIx calculated at 60, 70, 170 and 180 min. The mean value and error bars are shown ($n = 7$). Data are presented as mean ± s.d. (iv) Parkes error grid of microneedle versus BGM (106 points) and (v) CGM versus BGM (72 points) with all glucose-monitoring data (Supplementary Fig. 24). A–E represent different zones. **b**, Simultaneous monitoring of ISF glucose, alcohol and lactate levels, along with BP, HR and AIx, for 400 min with intake of a meal at 20 min, an alcoholic drink at 80 min and 20 min of vigorous-intensity exercise at 200 min in a healthy participant. (i) The participant acquired ISF glucose levels, alcohol levels and lactate levels along with BP and HR over 400 min. Blood glucose and lactate levels were measured via a blood meter every 20 min, while alcohol levels were measured via a breathalyser every 20 min. The additional points were measured every 10 min, from 80 to 120 min for alcohol, and every 10 min from 200 to 240 min for lactate and glucose. The participant acquired ISF glucose levels, alcohol levels and lactate levels, along with BP and HR, over 400 min. Blood glucose and lactate levels were measured via a blood meter every 20 min, while alcohol levels were measured via a breathalyser every 20 min. The additional points were measured every 10 min, from 80 to 120 min for alcohol, and every 10 min from 200 to 240 min for lactate and glucose. (ii) The 8 s BP data recorded at 20, 30, 80, 90, 200, 220 and 240 min during the different intakes and stimulations. (iii) AIx calculated at 20, 30, 80, 90, 200, 220 and 240 min, which is before and after each stimulation, with mean value and error bars ($n = 7$). Data are presented as mean ± s.d. (iv) Correlation of the total 90 paired microneedle alcohol measurements versus a commercial breathalyser. (v) Correlation of the total 123 paired microneedle lactate measurements versus blood lactate measurements taken on the commercial meter. (vi) Correlation of the total 175 paired SBP and DBP measurements based on the US sensor versus a commercial BP device.

(71 paired data points with blood meter), while the MARD compared to blood was 3.70% (158 paired data points with blood meter). The increasing BP and HR after the meal can be attributed to an increased blood supply. Splanchnic oxygen is increasingly consumed by the gastrointestinal tract for digestive activities, which increases the blood flow rate to support the oxygen requirements[39]. Similarly, intake of caffeine-containing iced tea stimulates the central nervous system and leads to higher heart contractility, HR and BP.

The BLUE platform provides continuous simultaneous multichannel sensing based on microneedles for glucose, lactate and alcohol, and ultrasound transducers and electrodes for BP, HR and arterial stiffness (Fig. 5b(i–iii)). This allows us to assess the interacting chemical–physical response to different stimulations. We studied the correlations between the dynamically changing levels of the three different biomarkers and the physiological signals during diverse daily activities over 6.5 h. The results show that ingestion of a meal (at 30 min) increased the glucose and BP levels while reducing the AIx (increased arterial stiffness). Consuming a glass of sugar-rich alcohol (at 85 min) led to increasing glucose and alcohol levels, as well as higher BP. Food in the stomach accounts for the decreasing alcohol adsorption rate[40]. Twenty minutes of vigorous-intensity exercise (2 h after the alcohol intake, 0.78 J s^{-1}) led to a notable increase in the lactate level, BP and HR, while reducing the glucose level to 66 mg dl^{-1} and increasing the AIx. In addition, consumption of different caffeine drinks (containing 200, 114 and 75 mg caffeine) and of ice cream (Supplementary Fig. 27) also stimulated the BP and HR (Supplementary Fig. 28). These results illustrate that caffeine intake has different effects on different individuals. Figure 5b(iv–v) shows the accuracy of the individual biomarker microneedle signals versus commercially measured data obtained with a blood lactate meter and breathalyser, while Fig. 5b(vi) shows the accuracy of the ultrasound BP measurements versus a commercial arm BP monitor. The corresponding r^2 values for the BP, alcohol and lactate data (0.98, 0.98 and 0.98, respectively) reflect the high accuracy and linearity of the BLUE platform compared with established gold standards.

Asymptomatic individuals, who may be at high risk for prediabetes did not perceive any symptoms or feel unwell, further highlighting the importance of this multimodal sensor. In addition, the population with prediabetes has a 50% risk of developing diabetes within five years and faces high risks of related chronic conditions, similar to diabetes stages[41]. Participants at high-risk of prediabetes were diagnosed based on one of two conditions: (1) impaired glucose tolerance with a glucose level 2 h post-meal of 140–199 mg dl^{-1} or (2) impaired fasting glucose with a fasting glucose level of 100–125 mg dl^{-1} (refs. 42–44).

Figure 6 illustrates the influence of daily activities, such as meals, alcohol consumption and exercise on blood lactate levels, correlating these activities with the lactate generation and clearance rates of each participant. After a meal, participants 1 (Fig. 6a) and 2 with high-risk prediabetes (Fig. 6b) exhibit glucose levels of 168 mg dl^{-1} (BP 160/104 mm Hg) and 240 mg dl^{-1} (BP 127/66 mm Hg), respectively, along with elevated lactate levels. Following alcohol consumption, participant 2 (Fig. 6b) shows lower glucose levels accompanied by higher blood lactate, HR and BP. In addition, 140 min post-meal, the glucose levels of participant 2 remained above 140 mg dl^{-1} (Supplementary Discussion 9). Participants with high-risk prediabetes experienced a greater influence of their daily activities on their blood lactate levels. Blood lactate level is an early marker for prediabetes, related to insulin resistance[45], with metabolic inflexibility reducing the lactate clearance rate[46]. However, exercise can improve insulin sensitivity[47], reduce blood glucose levels and lower BP. Participant 1 with high-risk prediabetes (Fig. 6a) showed a decrease in BP from 137/99 mm Hg (initial baseline) to 129/77 mm Hg (new baseline) after 20 min of vigorous-intensity exercise (0.82 J s^{-1}).

Comparing participants with high-risk prediabetes (Fig. 6 and Supplementary Fig. 29) and the healthy participant in Fig. 5b, the healthy individual maintained stable lactate levels during the consumption of meals and alcohol, with lactate levels returning to baseline within 30 min post-exercise. In addition, the healthy participant exhibited a rapid response with blood glucose levels reducing to the normal range (116.4 mg dl^{-1}, 40 min post-meal). By contrast, participants with high-risk prediabetes demonstrated low lactate clearance rates, with elevated lactate during the intake of meals or alcohol, requiring more than 60 min to return to baseline after 20 min of exercise. The lactate clearance rate is influenced by body mass index, exercise frequency and health status. A higher body mass index is associated with high-risk prediabetes, characterized by a lower lactate threshold and lower lactate clearance rate[46,48] (Supplementary Table 2 and Supplementary Discussion 9). In addition, the BP of high-risk participants increased substantially during the consumption of meals or alcohol and remained approximately 10 mm Hg higher (Supplementary Discussion 9).

Individuals with prediabetes (Fig. 6 and Supplementary Fig. 29, discussed in Supplementary Discussion 9) experience health conditions and issues similar to people with diabetes, including high BP, lower lactate clearance and increased arterial stiffness. Lactate levels, BP and arterial stiffness are greatly influenced by meals, drinks and exercise. Elevated lactate levels can harm the body by decreasing blood pH, and cause serious damage to organs[49,50]. In addition, high BP and arterial stiffness are diabetes-related indicators of cardiovascular risks. The BLUE system addresses several critical gaps in the current management of prediabetes and diabetes. First, it provides rapid feedback on the effect of lifestyle changes, helping to maintain motivation[51]. Second, its ability to quantify improvements in metabolic and physiological signals offers users instant gratification[52]. Third, it provides timely alerts for early intervention to prevent the progression from prediabetes to diabetes[53]. Finally, it collects personalized multisource rich data to generate customized disease management plans[54].

The real-time multimodal platform offers individuals with high-risk diabetes the opportunity to modify their lifestyles through feedback that reflects changes in their health status. The system offers tracking capabilities for patients with prediabetes and diabetes, enabling them to manage their insulin dosing, along with timely dietary and lifestyle interventions, based on the rich real-time multisource data. It provides tailored personalized recommendations for diet, exercise and daily activities, along with real-time feedback to prevent significant fluctuations in blood glucose, lactate levels, BP and arterial stiffness. Unlike in healthy individuals, fluctuations in glucose, lactate, BP and arterial stiffness can lead to severe complications for people with diabetes, such as stroke, kidney disease and amputations. However, there is no one-size-fits-all treatment for diabetes. Each patient has unique health issues. For example, the three participants with high-risk prediabetes experienced different levels of progressive conditions (Fig. 6). Generating and processing their dynamic multisource data offers the opportunity for predicting abnormalities and personalizing their disease management.

Continuous multi-parameter monitoring can facilitate understanding of the influence of diverse daily activities on individual's biosignals and health (Fig. 5b). The correlation between the different sensor outputs and the participant's activities can be visualized in a chord diagram (Supplementary Fig. 30). Such a diagram supports understanding of the interplay between ISF biomarkers with physical signals during different activities and potentially enables personalized interventions that enhance one's health and wellness (Supplementary Discussion 8).

Discussion

The study aims to showcase that integrating multiple chemical and physical sensors in a single wristband addresses several critical gaps in managing prediabetes and diabetes beyond traditional CGM-based diabetes management. By providing continuous comprehensive metabolic and cardiovascular sensing, the multimodal BLUE platform holds considerable promise for advancing personalized diabetes management

https://doi.org/10.1038/s41551-025-01439-z

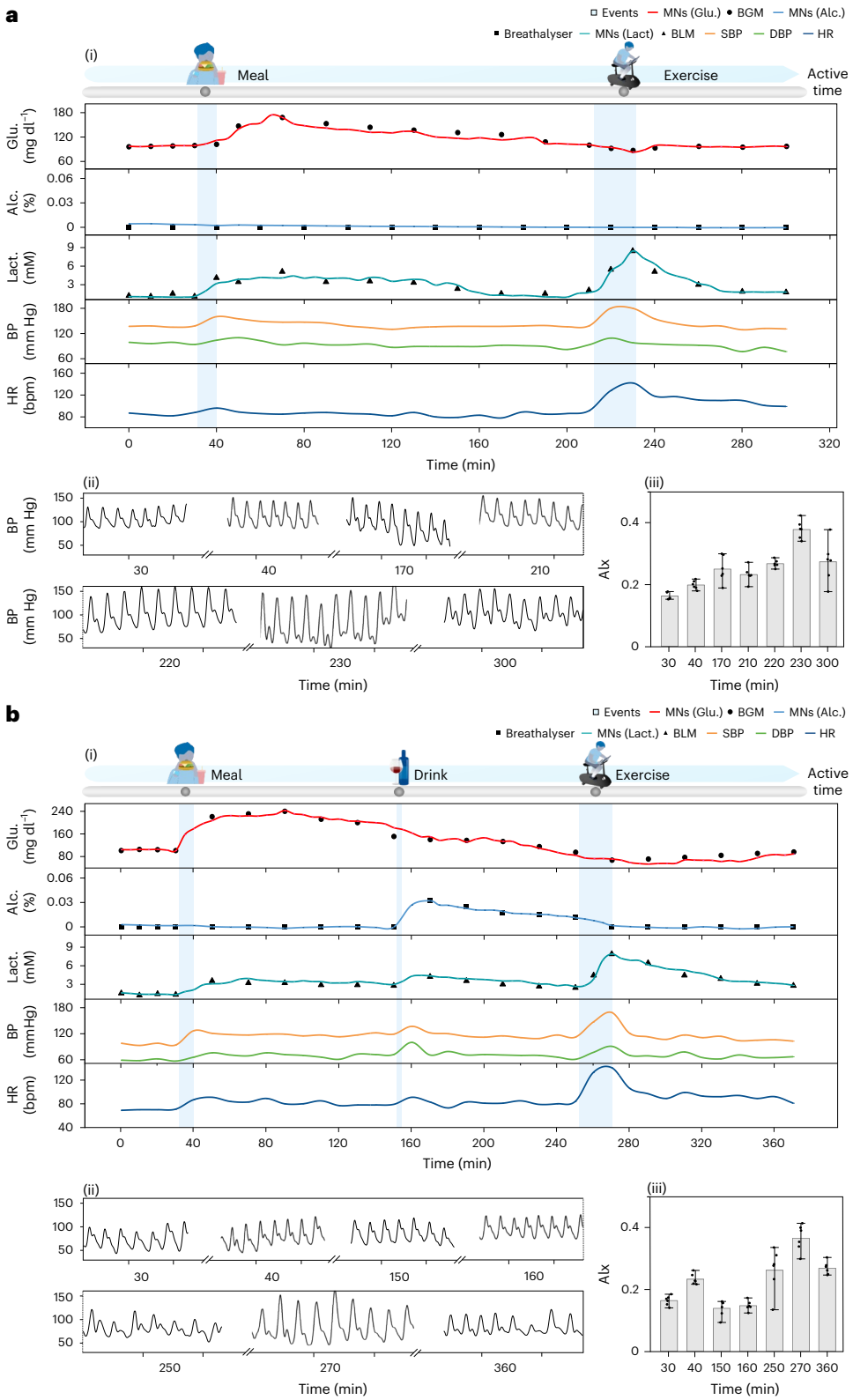

Fig. 6 | Extended simultaneous in vivo monitoring of BP along with multiple biomarkers in high-risk prediabetes during different daily activities. **a**, Participant 1 with high-risk prediabetes. (i) ISF glucose, BP and HR parameters were recorded over a period of 300 min. After 30 min of baseline, a meal is taken, followed by exercise at 210 min. The wristband results were compared with measurements of a commercial BGM at 20 min and of an arm BP cuff at 10 min (upper). (ii) BP signals, each lasting 8 s, were recorded at 30, 40, 170, 210, 220, 230 and 300 min. (iii) Arterial stiffness, represented by AIx values, was calculated at 30, 40, 170, 210, 220, 230 and 300 min ($n = 6$) and data are presented as mean ± s.d. **b**, Participant 2 with high-risk prediabetes 2. (i) ISF glucose, BP and HR parameters were recorded over a period of 370 min. Food consumption occurred after 30 min of baseline measurements, followed by drinking at 150 min and exercise at 250 min. The wristband results were compared with measurements of a commercial BGM at 20 min and of an arm BP monitor at 10 min (upper). (ii) BP signals, each lasting 8 s, were recorded at 30, 40, 150, 160, 250, 270 and 360 min. (iii) Arterial stiffness, as represented by AIx values, was calculated at 30, 40, 150, 160, 250, 270 and 360 min ($n = 6$) and data are presented as mean ± s.d.

and maintaining glycaemic control while alerting for cardiac risks. The wristband hybrid system offers highly accurate continuous monitoring of multiple metabolites beyond glucose and cardiac physiological signals affecting the pathophysiology of diabetes and associated with related cardiovascular risks. Such simultaneous real-time ultrasound and electrochemical sensing, combined with advanced data processing, would facilitate more comprehensive disease diagnostics, early prediction and timely alerts of abnormal physiological changes. The individual electrochemical and ultrasound sensing modalities of the hybrid platform offer excellent sensitivity, selectivity, reproducibility and accuracy (without crosstalk) to support understanding of the correlation and interplay between ISF biomarkers and physical signals during diverse daily activities. This 'all-in-one' multiplexed chemical–physical wearable health-monitoring device provides useful rich multisource insights into the comprehensive physiological status and glycaemic variability of individuals towards optimal closed-loop insulin-delivery systems and enhanced management of diabetes and other chronic diseases, greatly beyond the limited chemical data of single-modality CGM devices. Fabricated SU-8 biocompatible microneedles have advanced the progress and performance of on-body signals. Integration of flexible microneedles and ultrasound sensors offers rich transient physio-metabolic profiles, relevant to hypertension during hyperglycaemia, post-exercise hypoglycaemia and elevated lactate from diabetic lactic acidosis, during diverse activities along with real-time feedback. The BLUE sensing platform is currently driven by external circuits and equipment (that is, potentiostat, pulse-receiver and BioRadio) that is powered separately (Supplementary Discussion 10 and Supplementary Figs. 31 and 32). This technology could be powered via a fully integrated circuit with rechargeable batteries, wireless data transfer via Bluetooth[12] and Wi-Fi[55] to electronic devices. The total estimated power consumption of the multimodal sensor is 617.92 mW. However, further efforts are needed on sustainable flexible printed circuit boards, which rely on the fabrication of rechargeable and flexible batteries, optimization of the system miniaturization, Bluetooth power consumption, crosstalk limitation and comfortable wearing.

Outlook

The multimodal BLUE platform provides continuous comprehensive metabolic and cardiovascular sensing for advancing personalized diabetes management, improving glycaemic control and alerting for cardiac risks. Although microneedle arrays offer tremendous promise for parallel measurements of multiple ISF biomarkers, their chemical diagnostic power is greatly enhanced by simultaneously measuring key physical signals, such as BP, HR and arterial stiffness. Looking to future developments of the multimodal wristband we expect several key directions: (1) large-scale clinical trials and extensive validation using people with T1D with changing meal plans and diverse physical activities to ensure the effectiveness and reliability of the device in real-world settings; (2) wearing the hybrid wristband over extended periods and incorporating it into the data science to provide early prediction of disorders and diseases; (3) full system integration of the multisource device, including an electronic interface for controlling the different sensing modalities, along with the batteries and data-transfer system; (4) expansion to additional diabetes-related biomarkers, such as ß-hydroxybutyrate, cortisol, insulin and potassium; (5) expansion to individuals with obesity who have a high prevalence of diabetes and cardiovascular disease; (6) monitoring additional physical vital signs, such as temperature and oxygen saturation; (7) combining with advanced machine learning clustering algorithms to predict abnormalities, health trends and future events and support closed-loop operations; and (8) pairing with additional chemical and physical sensors, depending on the specific user (for example, target disease or population). By adding more chemical–physical sensing parameters, and coupling with advanced data processing, the new multiplexed health-monitoring platform would offer rich multisource insights into the comprehensive health status of individuals towards guiding personalized interventions and managing chronic diseases. Achieving full system integration is the ultimate objective for this powerful multisource device. Although full integration of the hybrid sensors with power storage and data processing, transmission and visualization components into a near-commercial product was not demonstrated in this work, we believe that this study has illustrated the tremendous promise and significance of a wearable platform—with multiple metabolite and vital sign sensing modalities—beyond current glucose-sensing based diabetes monitoring.

Methods

Materials and chemicals

Acetaminophen, alcohol oxidase solution from *Pichia pastoris* (40 U mg^{-1}), L-ascorbic acid, bovine serum albumin (BSA) from lyophilized powder, calcium chloride anhydrous, chitosan (medium molecular weight), disodium hydrogen phosphate, pure ethanol (200 proof), glacial acetic acid (HOAc), γ-globulins from bovine blood, D-(+)-glucose anhydrous, glucose oxidase from *Aspergillus* (142,838 U g^{-1}), glutaraldehyde, L-lactic acid, magnesium sulfate anhydrous, PBS (1.0 M, pH 7.4), polyvinyl chloride, potassium chloride, sodium bicarbonate, NaCl, $NaH_2PO_4{\cdot}2H_2O$, silver flakes, tetrahydrofuran, Titron X-100 solution, toluene and uric acid were purchased from Sigma-Aldrich. Lactate oxidase (111 U mg^{-1}) was purchased from Toyobo Corp. All aqueous solutions were prepared using doubly deionized water. PDMS Sylgard 184 silicone elastomer (Ellsworth Adhesives) and SU-8 2100 were provided by WPI and Kayakli, respectively. Biocompatible BioMed photocurable resin (clear resin) was purchased from Formlabs, while the flexible photocurable resin (white UV tough resin) was purchased from Anycubic. Styrene–ethylene–butylene–styrene (SEBS) G1645 and MD1648 tri-block copolymers were obtained from Kraton. Custom stainless steel stencils were ordered from Metal Etch Services. Ecoflex (part A and part B) were purchased from Smooth-On, Inc. All reagents and solvents were used without further modification and purification.

Fabrication of flexible microneedle patch

The microneedles were designed in SolidWorks and printed in a Formlabs 3D printer (model: Form 3, resolution 25 µm). After the printing procedure, the 3D-printed microneedles were washed in an isopropanol bath, following by a post-curing step under a UV lamp (Form Cure, Formlabs) for 1 h (Supplementary Fig. 3a).

The silicone elastomer kit was mixed with the curing agent in a ratio of 10 to 1. The mixed PDMS was cast into the 3D-printed microneedles attached to a glass Petri dish, which was then degassed in a vacuum pump for 30 min at 762 mm Hg. PDMS mould was cured for 60 min at 60 °C (Supplementary Fig. 3b,c).

The SU-8 solution was poured into the PDMS mould and degassed in a vacuum pump for 10 min. After the SU-8 was cured under a UV lamp (Black Ray Lamp, model UVL-21, wavelength 365 nm), the PDMS moulds were detached from the SU-8 microneedles and the microneedles were attached to glass slides by soft lithography for further processing (Supplementary Fig. 3d). The prepared SU-8 microneedles were etched using plasma dry etching for 60 min to increase tip sharpness, the soft lithography step was then repeated to attach the etched microneedle to the tape (Supplementary Fig. 3e–h).

The 3D-printed masks were attached to the microneedle using a design comprising four separated electrodes. Before sputtering, the microneedles were cleaned using a nitrogen gun and attached to the sample stage. Microneedles were sputtered first with a Cr film of 188.40 ± 26.87 µm followed by a Pt film of 337.76 ± 44.08 µm using a Denton Discovery 635 sputtering system (Supplementary Fig. 3i).

Preparation of the silver inks

A homemade stretchable silver ink was used for the circuit connections to various components of the wristband. The ink included silver flakes,

SEBS resin (G1645, 4 g in 10 ml of toluene) and toluene at a weight ratio of 4:2:1. A homogeneous composition was obtained using a planetary mixer (FlackTek, SpeedMixer DAC 150.1 FVZ) at 1,800 rpm for 10 min.

Fabrication of the wristband

The SEBS substrate was prepared by dissolving MD1648 tri-block copolymers in toluene (40 wt%) and mixing on a linear shaker (Scilogex, SK-L 180-E). The SEBS blend was then cast onto a polyethylene terephthalate sheet using a doctor blade to achieve a thickness of 300 µm, followed by curing at ambient temperature for 1 h.

The wristband circuit was designed on AutoCAD 2023 (Autodesk) and patterned onto a custom stencil (Metal Etch Services). The circuit connection was fabricated by screen-printing the formulated silver ink onto the SEBS substrate using the stencil. A chloride–lactate treatment, adapted from a previous study[56], enhanced conductivity and stability. Briefly, the treatment involved spraying the aqueous solution (containing 100 mM NaCl and 50 mM lactic acid) evenly onto the silver pattern and drying it in the oven at 80 °C for 5 min for a total of three rounds[57]. Afterwards, a washing step with distilled water was conducted, followed by curing in the oven at 80 °C until thoroughly dried.

Fabrication of the ECG sensor

The ultrasound rods were assembled on the wristband using a solvent-welding process, which enables firm bonding between parts with different elastic moduli. A 2-µl droplet of a toluene–ethanol mixture (3:7 v/v) was applied to the designated position to partially dissolve the silver connections and SEBS, allowing mounting of the ultrasound rods onto the substrate. The solvent was then allowed to evaporate at room temperature, facilitating the re-crosslinking of SEBS to secure welding of the substrate and silver inks to the ultrasound rods. Subsequently, a top layer of silver interconnections was adhered to the ultrasound rods and sealed with Ecoflex rubber. This was followed by curing in the oven at 60 °C for 30 min. Finally, the external circuit connector was solvent-welded using a 10 µl toluene–ethanol mixture onto the SEBS substrate in a similar fashion.

Microneedle modification

Modification of the three different microneedle working electrodes (glucose, lactate and alcohol) relied on a drop cast layer-by-layer technique[58]. The enzymes solutions, glucose oxidase (5 U µl^{-1}) for glucose and lactate oxidase (12 U µl^{-1}) for lactate, were prepared in BSA (10 mg ml^{-1} in 0.1 M PBS). For alcohol, the enzyme (alcohol oxidase, final concentration 4 U µl^{-1}) was mixed with BSA (10 mg ml^{-1} in 0.1 M PBS) and chitosan (1 wt% in 0.1 M HOAc) at a ratio 2:1:1 (refs. 12,59). Five layers (4 µl) of each enzyme solution were successively drop cast on top of the microneedles. For glucose and lactate microneedle sensors, two extra layers were added (4 µl): a solution of 2 v/v% glutaraldehyde in distilled water followed by a 1% chitosan solution (in HOAc 0.1 M). Finally, in all working microneedles, a protective layer consisting in a solution of 2 wt% polyvinyl chloride (in tetrahydrofuran with 1 mM Triton X-100) was cast to avoid leaching and biofouling problems. After modification, the patches were stored overnight in the fridge (4 °C) for further in vitro and on-body testing.

Calibration of the arterial blood pressure waveform

The BP waveform was calibrated using equation (1), where p_d is the diastolic pressure, A_d is the diastolic arterial cross-sectional area and α is the rigidity coefficient. The arterial BP waveform, denoted $p(t)$, is described as[26]:

$$p(t) = p_d \times e^{\alpha\left(\frac{A(t)}{A_d} - 1\right)} \tag{1}$$

Given the assumption of rotational symmetry in the arterial structure, the arterial cross-sectional area is denoted as $A(t)$, with $d(t)$ representing the diameter waveform of the specific target artery, computed as:

$$A(t) = \frac{\pi d(t)^2}{4} \tag{2}$$

It can be assumed that human blood vessels exhibit an elastic behaviour with minor viscoelastic effects. This implies that the relationship between pressure and vessel diameter demonstrates a relatively modest hysteresis effect, which is below 0.2% (ref. 60). Equation (1) can be used effectively to reconstruct precise arterial BP waveforms based on vessel diameter waveforms.

Equation (3) can be used to calculate α, where A_s is the systolic arterial cross-section and p_s, representing the systolic pressure, can be measured by a US Food and Drug Administration-approved BP cuff.

$$\alpha = \frac{A_d \ln(p_s - p_d)}{A_s - A_d} \tag{3}$$

An accurate value of $p(t)$ can be obtained using equation (1) with calibrated α and p_d and carefully measured $d(t)$ (vessel diameter) values. The accuracy of the measured $d(t)$ can be evaluated by utilizing a clinical ultrasonic machine to capture the systolic diameter at the same vascular location.

Blood pressure calibration coefficient

Every waveform presented in this study has been adjusted using a commercial pressure cuff for calibration. As long as the participant has not undergone any significant physiological changes or vascular reconstructions, calibration of the device only has to be done once, because even though pulse pressure may vary from one heartbeat to another, diastolic pressure remains relatively consistent under stable physiological conditions.

According to equations (1) and (2), the connection between the measured signal, arterial diameter and BP value can be described as:

$$\ln p(t) = (\ln p_d)\,\alpha\left[\frac{d(t)^2}{d_D^2} - 1\right] \tag{4}$$

In this context, d_D is the minimum diameter observed in a single cardiac cycle (Supplementary Fig. 24), which corresponds to the diastolic blood pressure. The actual value, represented as $\ln p(t)$, is directly related to the signal $\frac{d(t)^2}{d_D^2} - 1$. The calibration coefficient, denoted as f, can be defined as the ratio between these two values:

$$f = \frac{\ln p(t)}{\frac{d(t)^2}{d_D^2} - 1} = (\ln p_d)\,\alpha \tag{5}$$

The calibration coefficient f is influenced by two parameters: the diastolic pressure p_d and the rigidity coefficient α. These two parameters can vary between different participants and need to be recalibrated each time the physiological state changes, such as when relaxing or exercising. The rigidity coefficient can be calibrated as given in equation (3). As the blood travels through the arterial tree, it is observed that the rigidity coefficient (α) and diastolic pressure (p_d) do not undergo substantial changes. Consequently, calibration of the brachial artery allows for the acquisition of BP waveforms at various positions, including the wrist, neck and foot in the same participant. In different scenarios, as long as α and p_d remain relatively stable, frequent recalibration of the device is unnecessary.

Arterial stiffness measurement

During various daily activities, the BP waveform contour exhibits fluctuations caused by variations in the systolic peak to reflected peak values. These differences are the result of differing levels of arterial stiffness. The variation in arterial stiffness is represented by distinct

reflected pulse levels from the distal ends of the arterial tree (Supplementary Fig. 25).

To assess arterial stiffness, the pulse wave decomposition analysis method is used[61,62]. This allows us to decompose pulse waveforms into forward waves, generated by the heartbeat, and reflected waves, which can be considered back-propagations from the distal ends of the arterial tree. A compliant or 'soft' artery tends to dilate more easily, leading to weaker reflections and slower back-propagation because of the lower impedance of the arterial tree. Consequently, this manifests as a weaker or delayed secondary peak in the pulse waveform. By contrast, a strong and rapidly occurring secondary peak indicates stiffer arterial networks with higher impedance. Here, we use AIx to discern the differences between the two peaks in the waveform.

$$\mathrm{AIx} = \frac{P_1 - P_2}{P_1} \times 100\% \tag{6}$$

where P_1 is the systolic peak and P_2 is the secondary or reflected peak. In our study, we conducted a beat-to-beat analysis of the BP waveform. This analysis allows us to calculate the beat-to-beat AIx, which is then averaged to reduce the potential error rate caused by waveform distortion.

Current conversion to concentration quantitation

Converting the microneedle current response to the blood concentration was achieved using equations correlating the I_b and I_M signals related to the metabolite concentrations measured using commercial blood meters, where I_b is the current reading at baseline and I_M is the reading on the maximum value.

Monitoring accuracy

The absolute relative difference (ARD) and the MARD value or CGM data accuracy were calculated from equations (7) and (8)[12]:

$$\mathrm{ARD}_t = \frac{|\mathrm{MN}_t - R_t|}{R_t} 100\% \tag{7}$$

$$\mathrm{MARD} = \frac{1}{N}\sum_{t=0}^{n} \mathrm{ARD}_t \tag{8}$$

Where t is the monitoring time point (every 5 min for CGM and every 10 min for BGM), MN_t is the microneedle glucose value measured at the time point, R_t is the reference glucose value measured at the time point (CGM or BGM values) and N is the total number of data measurement sets of MN to R.

Data collection and transfer

Micro-coax wires were used to connect the microneedles from the wristband to the potentiostat (SensitBT) and digital data were transferred via Bluetooth to the computer (PSTrace v.5.9 software). The ECG pad was adapted to a micro-coax wire and connected to the electric transducer (BioRadio) and digital data were transferred via Bluetooth to the computer (Biocapture software). The ultrasound sensor was adapted to a micro-coax wire and connected to a pulser–receiver (Olympus 5072PR) wire connected to the computer for data collection (LabView 2018 software).

Statistics and reproducibility

On-body measurements were conducted in 11 healthy participants. Each individual calibration was followed by the current conversion to concentration discussed above. After collecting all data, r^2 indicated the high accuracy of the sensor separately for each target analyte: for alcohol with 90 points, lactate with 123 points, glucose with 158 points and BP with 175 points. All data were paired with measurements using commercial devices.

MARD and the Parkes errors grid were used to assess the clinical accuracy of the on-body measurements (versus gold standard assays). The MARD value of alcohol is 8.84% compared with a commercial breathalyser (26 paired data points), the MARD value of lactate is 7.97% compared with a commercial lactate blood meter (26 paired data points), the MARD value of CGM is 6.58% compared with a commercial glucose blood meter (71 paired data points), and the MARD value of microneedles glucose is 3.7% compared with a commercial glucose blood meter (158 paired data points).

For the mechanical bending test (Fig. 2), the error bar was used to evaluate the flexible structural stability with a sample size of $n = 5$. For arterial stiffness (Figs. 4 and 5 and Supplementary Figs. 26–30), the error bar was used to evaluate AIx values plotted as the mean value using a sample size of $n = 7$. No data were excluded from the analysis.

For in vitro experiments (Supplementary Figs. 18 and 19), the error bar was used to evaluate the reproducibility of alcohol, lactate and glucose with a sample size of $n = 3$. No data were excluded from the analysis.

Reporting summary

Further information on research design is available in the Nature Portfolio Reporting Summary linked to this article.

Data availability

The manuscript includes all the data collected and analysed in the study, and more information is included in the Supplementary Information.

Code availability

The code for decoding the transducer data to blood pressure waveforms is available via GitHub at https://github.com/MuyangLin95/Processing-scripts-for-monitoring-metabolites-and-cardiac-signals-in-diabetes.git (ref. 63).

References

1. Zimmet, P. Z., Magliano, D. J., Herman, W. H. & Shaw, J. E. Diabetes: a 21st century challenge. *Lancet Diabetes Endocrinol.* **2**, 56–64 (2014).
2. Roglic, G. WHO Global report on diabetes: a summary. *Int. J. Noncommun. Dis.* **1**, 3–8 (2016).
3. Klonoff, D. C., Ahn, D. & Drincic, A. Continuous glucose monitoring: a review of the technology and clinical use. *Diabetes Res. Clin. Pract.* **133**, 178–192 (2017).
4. Lin, R., Brown, F., James, S., Jones, J. & Ekinci, E. Continuous glucose monitoring: a review of the evidence in type 1 and 2 diabetes mellitus. *Diabet. Med.* **38**, e14528 (2021).
5. Teymourian, H., Barfidokht, A. & Wang, J. Electrochemical glucose sensors in diabetes management: an updated review (2010–2020). *Chem. Soc. Rev.* **49**, 7671–7709 (2020).
6. Wolkowicz, K. L. et al. A review of biomarkers in the context of type 1 diabetes: biological sensing for enhanced glucose control. *Bioeng. Transl. Med.* **6**, e10201 (2020).
7. Avogaro, A. et al. Glucose tolerance during moderate alcohol intake: insights on insulin action from glucose/lactate dynamics. *J. Clin. Endocrinol. Metab.* **87**, 1233–1238 (2002).
8. Zhou, M.-S., Wang, A. & Yu, H. Link between insulin resistance and hypertension: what is the evidence from evolutionary biology? *Diabetol. Metab. Syndr.* **6**, 12 (2014).
9. Svensson, M. K. et al. Alterations in heart rate variability during everyday life are linked to insulin resistance. A role of dominating sympathetic over parasympathetic nerve activity? *Cardiovasc. Diabetol.* **15**, 91 (2016).
10. Eckel, R. H., Bornfeldt, K. E. & Goldberg, I. J. Cardiovascular disease in diabetes, beyond glucose. *Cell Metab.* **33**, 1519–1545 (2021).

11. Chen, Y., Lee, K., Ni, Z. & He, J. C. Diabetic kidney disease: challenges, advances, and opportunities. *Kidney Dis.* **6**, 215–225 (2020).
12. Tehrani, F. et al. An integrated wearable microneedle array for the continuous monitoring of multiple biomarkers in interstitial fluid. *Nat. Biomed. Eng.* **6**, 1214–1224 (2022).
13. Tasca, F., Tortolini, C., Bollella, P. & Antiochia, R. Microneedle-based electrochemical devices for transdermal biosensing: a review. *Curr. Opin. Electrochem.* **16**, 42–49 (2019).
14. Himawan, A. et al. Where microneedle meets biomarkers: futuristic application for diagnosing and monitoring localized external organ diseases. *Adv. Healthc. Mater.* **12**, 2202066 (2023).
15. Imani, S. et al. A wearable chemical–electrophysiological hybrid biosensing system for real-time health and fitness monitoring. *Nat. Commun.* **7**, 11650 (2016).
16. Xu, Y. et al. In-ear integrated sensor array for the continuous monitoring of brain activity and of lactate in sweat. *Nat. Biomed. Eng.* **7**, 1307–1320 (2023).
17. Sempionatto, J. R. et al. An epidermal patch for the simultaneous monitoring of haemodynamic and metabolic biomarkers. *Nat. Biomed. Eng.* **5**, 737–748 (2021).
18. Xu, C. et al. A physicochemical-sensing electronic skin for stress response monitoring. *Nat. Electron.* **7**, 168–179 (2024).
19. Bernardin, G., Pradier, C., Tiger, F., Deloffre, P. & Mattei, M. Blood pressure and arterial lactate level are early indicators of short-term survival in human septic shock. *Intensive Care Med.* **22**, 17–25 (1996).
20. Ho, K. K. Y. et al. Evaluation of an anti-thrombotic continuous lactate and blood pressure monitoring catheter in an in vivo piglet model undergoing open-heart surgery with cardiopulmonary bypass. *Chemosensors (Basel)* **8**, 56 (2020).
21. Moonla, C. et al. Continuous ketone monitoring via wearable microneedle patch platform. *ACS Sens.* **9**, 1004–1013 (2024).
22. Roh, H. et al. Fabrication of high-density out-of-plane microneedle arrays with various heights and diverse cross-sectional shapes. *Nanomicro. Lett.* **14**, 24 (2021).
23. Chang, A.-Y. et al. Dopamine sensing with robust carbon nanotube implanted polymer micropillar array electrodes fabricated by coupling micromolding and infiltration coating processes. *Electrochim. Acta* **368**, 137632 (2021).
24. Römgens, A. M., Bader, D. L., Bouwstra, J. A., Baaijens, F. P. T. & Oomens, C. W. J. Monitoring the penetration process of single microneedles with varying tip diameters. *J. Mech. Behav. Biomed. Mater.* **40**, 397–405 (2014).
25. MicroChem. *SU-8 2000.5-2015 Permanent Epoxy Negative Photoresist PROCESSING GUIDELINES. SU-8 2000 Datasheet* 1–5 (Kayaku, 2015).
26. Wang, C. et al. Monitoring of the central blood pressure waveform via a conformal ultrasonic device. *Nat. Biomed. Eng.* **2**, 687–695 (2018).
27. Gordin, D. et al. Influence of postprandial hyperglycemic conditions on arterial stiffness in patients with type 2 diabetes. *J. Clin. Endocrinol. Metab.* **101**, 1134–1143 (2016).
28. Carlson, O. et al. Impact of reduced meal frequency without caloric restriction on glucose regulation in healthy, normal-weight middle-aged men and women. *Metabolism* **56**, 1729–1734 (2007).
29. Clark, L. T. Alcohol-induced hypertension: mechanisms, complications, and clinical implications. *J. Natl Med. Assoc.* **77**, 385–389 (1985).
30. Mayl, J. J. et al. Association of alcohol intake with hypertension in type 2 diabetes mellitus: the ACCORD Trial. *J. Am. Heart Assoc.* **9**, e017334 (2020).
31. Howes, L. G. & Reid, J. L. The effects of alcohol on local, neural and humoral cardiovascular regulation. *Clin. Sci.* **71**, 9–15 (1986).
32. Hwang, C.-L., Muchira, J., Hibner, B. A., Phillips, S. A. & Piano, M. R. Alcohol consumption: a new risk factor for arterial stiffness? *Cardiovasc. Toxicol.* **22**, 236–245 (2022).
33. Tian, D. & Meng, J. Exercise for prevention and relief of cardiovascular disease: prognoses, mechanisms, and approaches. *Oxid. Med. Cell. Longev.* **2019**, 3756750 (2019).
34. Shahraki, M. R., Mirshekari, H., Shahraki, A. R., Shahraki, E. & Naroi, M. Arterial blood pressure in female students before, during and after exercise. *ARYA Atheroscler.* **8**, 12–15 (2012).
35. Coates, A. M., Joyner, M. J., Little, J. P., Jones, A. M. & Gibala, M. J. A perspective on high-intensity interval training for performance and health. *Sport Med.* **53**, 85–96 (2023).
36. Mohammed, L. L. M. et al. Exercise-induced hypertension in healthy individuals and athletes: is it an alarming sign? *Cureus* **12**, e11988 (2020).
37. MacDonald, J. R. Potential causes, mechanisms, and implications of post exercise hypotension. *J. Hum. Hypertens.* **16**, 225–236 (2002).
38. Parkes, J. L., Slatin, S. L., Pardo, S. & Ginsberg, B. H. A new consensus error grid to evaluate the clinical significance of inaccuracies in the measurement of blood glucose. *Diabetes Care* **23**, 1143–1148 (2000).
39. Madsen, J. L., Søndergaard, S. B. & Møller, S. Meal-induced changes in splanchnic blood flow and oxygen uptake in middle-aged healthy humans. *Scand. J. Gastroenterol.* **41**, 87–92 (2006).
40. Jones, A. W. & Jönsson, K. A. Food-induced lowering of blood-ethanol profiles and increased rate of elimination immediately after a meal. *J. Forensic Sci.* **39**, 1084–1093 (1994).
41. Richter, B. et al. Development of type 2 diabetes mellitus in people with intermediate hyperglycaemia. *Cochrane Database Syst. Rev.* **10**, CD012661 (2018).
42. Warren, B. et al. Comparative prognostic performance of definitions of prediabetes: a prospective cohort analysis of the Atherosclerosis Risk in Communities (ARIC) study. *Lancet Diabetes Endocrinol.* **5**, 34–42 (2017).
43. Huang, Y. et al. Association between prediabetes and risk of cardiovascular disease and all cause mortality: systematic review and meta-analysis. *BMJ* **355**, i5953 (2016).
44. Rooney, M. R. et al. Global prevalence of prediabetes. *Diabetes Care* **46**, 1388–1394 (2023).
45. Hu, J.-R. et al. Effects of carbohydrate quality and amount on plasma lactate: results from the OmniCarb trial. *BMJ Open Diabetes Res. Care* **8**, e001457 (2020).
46. Emhoff, C.-A.W. & Messonnier, L.A. Concepts of lactate metabolic clearance rate and lactate clamp for metabolic inquiry: a mini-review. *Nutrients* **15**, 3213 (2023).
47. Rynders, C. A. et al. Effects of exercise intensity on postprandial improvement in glucose disposal and insulin sensitivity in prediabetic adults. *J. Clin. Endocrinol. Metab.* **99**, 220–228 (2014).
48. Chai, Y. et al. Association of body mass index with risk of prediabetes in Chinese adults: a population-based cohort study. *J. Diabetes Investig.* **13**, 1235–1244 (2022).
49. Shapiro, N. I. et al. Lactate as a predictor of mortality in patients with severe sepsis. *Crit. Care Med.* **37**, 1678–1684 (2009).
50. Bishop, N. D. et al. The role of lactate in the assessment of the critically ill. *J. Criti. Care* **37**, 110–115 (2017).
51. Bodenheimer, T. & Handley, M. A. Goal-setting for behavior change in diabetes: what's the evidence? *Diabetes Educ.* **35**, 775–782 (2009).
52. Fisher, L. et al. The role of self-monitoring in diabetes management: a review. *Diabetes Spectrum* **29**, 129–135 (2016).
53. Tabák, A. G. et al. Prediabetes: a high-risk state for developing diabetes. *Lancet* **379**, 2279–2290 (2012).

54. Zhang, Y. et al. Artificial intelligence in diabetes care: current applications and future directions. *Diabetes Care* **43**, 141–148 (2020).
55. Lin, M. et al. A fully integrated wearable ultrasound system to monitor deep tissues in moving subjects. *Nat. Biotechnol.* **42**, 448–457 (2024).
56. Lv, J. et al. Printable elastomeric electrodes with sweat-enhanced conductivity for wearables. *Sci. Adv.* **7**, eabg8433 (2021).
57. Yin, L. et al. A stretchable epidermal sweat sensing platform with an integrated printed battery and electrochromic display. *Nat. Electron.* **5**, 694–705 (2022).
58. Kim, J. et al. Simultaneous monitoring of sweat and interstitial fluid using a single wearable biosensor platform. *Adv. Sci.* **5**, 1800880 (2018).
59. Kim, J. et al. Noninvasive alcohol monitoring using a wearable tattoo-based iontophoretic-biosensing system. *ACS Sens.* **1**, 1011–1019 (2016).
60. Butman, S. M., Ewy, G. A., Standen, J. R., Kern, K. B. & Hahn, E. Bedside cardiovascular examination in patients with severe chronic heart failure: importance of rest or inducible jugular venous distension. *J. Am. Coll. Cardiol.* **22**, 968–974 (1993).
61. Baruch, M. C., Kalantari, K., Gerdt, D. W. & Adkins, C. M. Validation of the pulse decomposition analysis algorithm using central arterial blood pressure. *Biomed. Eng. Online* **13**, 96 (2014).
62. Izzo, J. L. Pulse contour analysis and augmentation index: It's time to move beyond cuff blood pressure measurement. *Am. J. Hypertens.* **18**, 1S–2S (2005).
63. Chang, A.-Y. et al. Processing-scripts-for-monitoring-metabolites-and-cardiac-signals-in-diabetes. *Zenodo* https://doi.org/10.5281/zenodo.15476742 (2025).

Acknowledgements

This research is supported by the UCSD Center for Wearable Sensors (CWS). M.R. received support from the UC-MEXUS-CONAHCYT Doctoral Fellowship. We thank S. Suresh for assistance.

Author contributions

A.-Y.C., M.L., L.Y., M.R., S.X. and J.W. conceived and designed the research. A.-Y.C., M.L., L.Y. and M.R. conducted the experiments. A.-Y.C., M.L., L.Y., M.R., S.D., R.L., Y.D., A.C., G.P., Z.L., H.L. and N.A. performed the experiments. A.-Y.C., M.L., L.Y. and M.R. analysed the data. A.-Y.C., M.L., L.Y., M.R., S.X. and J.W. wrote the manuscript with valuable feedback and assistance from other co-authors.

Competing interests

The authors declare no competing interests.

Additional information

Supplementary information The online version contains supplementary material available at https://doi.org/10.1038/s41551-025-01439-z.

Correspondence and requests for materials should be addressed to Sheng Xu or Joseph Wang.

Peer review information *Nature Biomedical Engineering* thanks Chi Hwan Lee and the other, anonymous, reviewer(s) for their contribution to the peer review of this work.

nature portfolio

Corresponding author(s): Sheng Xu and Joseph Wang

Last updated by author(s): Mar 31, 2025

Reporting Summary

Nature Portfolio wishes to improve the reproducibility of the work that we publish. This form provides structure for consistency and transparency in reporting. For further information on Nature Portfolio policies, see our Editorial Policies and the Editorial Policy Checklist.

Statistics

For all statistical analyses, confirm that the following items are present in the figure legend, table legend, main text, or Methods section.

n/a	Confirmed	
☐	☒	The exact sample size (*n*) for each experimental group/condition, given as a discrete number and unit of measurement
☐	☒	A statement on whether measurements were taken from distinct samples or whether the same sample was measured repeatedly
☒	☐	The statistical test(s) used AND whether they are one- or two-sided *Only common tests should be described solely by name; describe more complex techniques in the Methods section.*
☒	☐	A description of all covariates tested
☒	☐	A description of any assumptions or corrections, such as tests of normality and adjustment for multiple comparisons
☐	☒	A full description of the statistical parameters including central tendency (e.g. means) or other basic estimates (e.g. regression coefficient) AND variation (e.g. standard deviation) or associated estimates of uncertainty (e.g. confidence intervals)
☒	☐	For null hypothesis testing, the test statistic (e.g. *F*, *t*, *r*) with confidence intervals, effect sizes, degrees of freedom and *P* value noted *Give P values as exact values whenever suitable.*
☒	☐	For Bayesian analysis, information on the choice of priors and Markov chain Monte Carlo settings
☒	☐	For hierarchical and complex designs, identification of the appropriate level for tests and full reporting of outcomes
☒	☐	Estimates of effect sizes (e.g. Cohen's *d*, Pearson's *r*), indicating how they were calculated

Our web collection on statistics for biologists contains articles on many of the points above.

Software and code

Policy information about availability of computer code

Data collection	SolidWorks (version of 2023 and 2024) was used for 3D designs, and the designs were printed on Formlabs 3D printer (Model: Form 3, resolution 25 µm). Commercial blood glucose meter (ACCU-CHEK), commercial blood lactate meter (NOVA Biomedical), and commercial breathalyzer (BACtrack S80 Pro) were used on each human participant to obtain blood correlation on glucose, lactate and breath alcohol data. Commercial blood pressure monitor OMRON BP7100 was used for blood pressure calibration. Electrochemical measurement were carry out by the SensitBT from PalmSens running a commercial software PSTrace5.9. For mechanical properties simulation, Comsol multiphysice version 6.1 was used. Ultrasound signals is acquired by Olympus 5072PR pulser-receiver running a customized script in LabView 2018. The biopotential signals were acquired by BioRadio running a commercial software Biocapture (version 5.6.7803.20370). The code for processing from the transducer raw data to blood pressure waveforms is available at https://github.com/MuyangLin95/Processing-scripts-for-monitoring-metabolites-and-cardiac-signals-in-diabetes.git
Data analysis	Origin pro was used to calculate statistical parameters. Comsol multiphysice 6.1 was used for mechanical properties simulation data processing.

For manuscripts utilizing custom algorithms or software that are central to the research but not yet described in published literature, software must be made available to editors and reviewers. We strongly encourage code deposition in a community repository (e.g. GitHub). See the Nature Portfolio guidelines for submitting code & software for further information.

Data

Policy information about availability of data

All manuscripts must include a data availability statement. This statement should provide the following information, where applicable:

- Accession codes, unique identifiers, or web links for publicly available datasets
- A description of any restrictions on data availability
- For clinical datasets or third party data, please ensure that the statement adheres to our policy

The manuscript includes all the data collected and analyzed in the study, and more information is included in the Supplementary Information.
The code for processing from the transducer raw data to blood pressure waveforms is available at https://github.com/MuyangLin95/Processing-scripts-for-monitoring-metabolites-and-cardiac-signals-in-diabetes.git

Human research participants

Policy information about studies involving human research participants and Sex and Gender in Research.

Reporting on sex and gender	From the eleven human participants, four are identify as Females and seven as Males.
Population characteristics	All healthy human participants are within the ages of 20-40.
Recruitment	The participating subjects of the study were recruited in a word-of-mouth manner from the UCSD campus. The participants recruited were healthy and were required to fill out an online qualification form before participating in the experiment. All participating subjects returned written informed consent before engaging in the experiment. There were no biases, such as self-selection and other biases.
Ethics oversight	Institutional Review Board at the University of California San Diego (#171927)

Note that full information on the approval of the study protocol must also be provided in the manuscript.

Field-specific reporting

Please select the one below that is the best fit for your research. If you are not sure, read the appropriate sections before making your selection.

☒ Life sciences ☐ Behavioural & social sciences ☐ Ecological, evolutionary & environmental sciences

For a reference copy of the document with all sections, see nature.com/documents/nr-reporting-summary-flat.pdf

Life sciences study design

All studies must disclose on these points even when the disclosure is negative.

Sample size	Fourteen healthy human participants were recruited for on body evaluation microneedles of the wristband, and eleven more participants were recruited for on body evaluation ultrasound and EEG of the wristband. Sample sizes were based on the standards of literature for proof-of-concept experiments.
Data exclusions	No data exclusion.
Replication	Following the protocol described in the manuscript, all attempts, including the fabrication and testing at replication, were successful.
Randomization	The wristband platform was fabricated and validated in the same process and was applied to all participating subjects in the same conditions. Thereby, randomization wasn't related to the study.
Blinding	Irrelevant. A blinding process would not affect the sampling results.

Reporting for specific materials, systems and methods

We require information from authors about some types of materials, experimental systems and methods used in many studies. Here, indicate whether each material, system or method listed is relevant to your study. If you are not sure if a list item applies to your research, read the appropriate section before selecting a response.

Materials & experimental systems

n/a	Involved in the study
☒	☐ Antibodies
☐	☒ Eukaryotic cell lines
☒	☐ Palaeontology and archaeology
☒	☐ Animals and other organisms
☒	☐ Clinical data
☒	☐ Dual use research of concern

Methods

n/a	Involved in the study
☒	☐ ChIP-seq
☒	☐ Flow cytometry
☒	☐ MRI-based neuroimaging

Eukaryotic cell lines

Policy information about cell lines and Sex and Gender in Research

Cell line source(s)	THP-1 cells were obtained from American Type Culture Collection.
Authentication	The cells were used without modification, as received from the supplier, and therefore were not authenticated.
Mycoplasma contamination	The cell line was tested monthly, and was negative for mycoplasma contamination.
Commonly misidentified lines (See ICLAC register)	No commonly misidentified cells were used.